



PS451 Final Year Project Report

A Theoretical Semi-Empirical Model for Precise Air Temperature Metrology

Paul McBrien

Student Number: 17715295

Programme: Applied Physics

Date: 13 April 2021

Supervisors:

Lampros Nikolopoulos, Dubhaltach MacLochlainn & Sam Boles

Declaration

Name: Paul McBrien

Student ID Number: 17715295

Programme: AP4

Module Code: PS451

Assignment Title: Final Year Project Literature Review

Submission Date: 12 April 2021

I understand that the University regards breaches of academic integrity and plagiarism as grave and serious. I have read and understood the DCU Academic Integrity and Plagiarism Policy. I accept the penalties that may be imposed should I engage in practice or practices that breach this policy. I have identified and included the source of all facts, ideas, opinions, viewpoints of others in the assignment references. Direct quotations, paraphrasing, discussion of ideas from books, journal articles, internet sources, module text, or any other source whatsoever are acknowledged and the sources cited are identified in the assignment references. I declare that this material, which I now submit for assessment, is entirely my own work and has not been taken from the work of others save and to the extent that such work has been cited and acknowledged within the text of my work. I have used the DCU library referencing guidelines, available at:

https://www.dcu.ie/library/classes_and_tutorials/citingreferencing.shtml

and/or the appropriate referencing system recommended in the assignment guidelines and/or programme documentation. By signing this form or by submitting this material online I confirm that this assignment, or any part of it, has not been previously submitted by me or any other person for assessment on this or any other course of study. By signing this form or by submitting material for assessment online I confirm that I have read and understood DCU Academic Integrity and Plagiarism Policy available at: <http://www.dcu.ie/registry/examinations/index.shtml>).

Name: Paul McBrien

Submission Date: 12 April 2021 i

Abstract

Recently, COVID-19 vaccines have required storage at temperatures as low as $-80\text{ }^{\circ}\text{C}$. Potential advances in areas such as quantum computing, alternative nuclear reactor technology and non-contact thermometry will likely require better precision for temperature measurements in gases such as air. It is therefore necessary to achieve lower uncertainties during temperature calibrations, especially for standard thermometers. The National Metrology Laboratory in Ireland have designed a submersible, stainless steel ‘torus’ as an alternative to climatic test chambers that can be used for air temperature calibrations. This project develops and investigates a thermodynamic model using empirical correlations and fluid dynamics equations. Computational fluid dynamics (CFD) simulations are used to verify the results of this theoretical model, which predicts that uncertainties can be reduced by up to 70 mK, a percentage reduction of over 69%. The model results are used to outline the optimal conditions for operating the torus as a temperature calibration system. Experimental work has been detailed with some engineering recommendations to overcome limitations posed by the torus design.

Acknowledgements

I would like to thank Dubhaltach MacLochlainn for his invaluable guidance and expertise throughout this project, and for ensuring I didn't lose my sanity during the engineering process. Also, thank you to Sam Boles for his erudite advice and patience in teaching me over the past year. I extend my gratitude to all staff at the National Metrology Laboratory and NSAI for giving me this opportunity and for providing me with the resources I needed.

I would also like Dr. Lampros Nikolopoulos for the helpful project advice and teaching through this year, and all my years in DCU. I would also like to thank Des Lavelle for taking the time to help with the engineering process. I also extend my gratitude to all the lecturers who helped me along the way.

Finally, thank you to my family and friends for supporting me over these past few years.

List of Figures

1	A glass SPRT with 405 mm probe length.	2
2	A capsule probe with 40 mm probe length.	3
3	Torus design diagrams.	5
4	Air dynamic viscosity and thermal conductivity graphs.	12
5	Kinematic viscosity graph.	13
6	Reynold's and Prandtl Number graphs.	14
7	Diametric error at 373.15 K.	15
8	Diametric error at 173.15 K.	16
9	Intermediary diametric error.	17
10	Zonal dependency graph for larger D	18
11	Zonal dependency graph for smaller D	19
12	Non-negligible length-error dependence.	20
13	Negligible sensor length-error dependence.	21
14	Sensor error-velocity dependence.	22
15	Smaller error variation across temperature range.	23
16	Larger error variation across temperature range.	24
17	3D CFD Model image.	28
18	Square root diametric error dependence CFD results.	30
19	Inverse square root diametric error dependence CFD results.	31
20	Inverse square diametric-error dependence CFD results.	32
21	Small emissivity zonal dependency graph.	34
22	Fan heating effect in the torus.	38
23	Gear and motor driven fan.	39
24	The gear-driven fan prototype.	40
25	Room temperature diametric error dependence.	49
26	Hot air diametric error dependence.	49
27	3D representation of all possible zonal dependency graphs.	50

Contents

1	Introduction	1
1.1	Temperature Metrology	1
1.2	Measurement Error and Uncertainty	1
1.3	Platinum Resistance Thermometers	2
1.4	Air Temperature Metrology	3
1.5	Project Aims	3
2	Theory and Background	4
2.1	Air Temperature Calibration Environment	4
2.2	Uncertainty Budgets	6
2.3	Thermodynamic Model Overview	6
2.4	Resistance Function Approximation	10
3	Analysis of the Theoretical Model	10
3.1	Torus Parameter Selection	10
3.2	Thermophysical Property Functional Approximation	11
3.3	Nusselt Number Analysis	13
3.4	Diametric Error Dependence	15
3.4.1	Contrary Square Root Dependences	15
3.4.2	Zonal Dependencies	18
3.5	Length Error Dependence	19
3.6	Velocity Error Dependence	21
3.7	Temperature Error Variation	22
4	Results and Discussion	24
4.1	Theoretical Model	24
4.2	CFD Results	27
4.2.1	Simulation 3D Model	27
4.2.2	ANSYS® Model Settings	28
4.2.3	Model Comparison	30
4.2.4	Theoretical Uncertainty Budgets	35
4.3	Pre-Lockdown Laboratory Work	36

4.3.1	Experimental Design	36
4.3.2	Initial Testing With Electric Fan	36
4.3.3	Internal Fan Heat Dissipation	37
4.3.4	Ball Bearing Freeze Test	38
4.3.5	Solutions	39
4.3.6	Gear-Driven Fan Design Process	39
4.3.7	Project Constraints and Solutions	40
4.3.8	Torus Heat Extraction	41
5	Conclusions and Future Perspectives	42

1 Introduction

1.1 Temperature Metrology

Temperature metrology is the practice and area of research associated with measuring temperature. This involves maintaining a repeatable measurement system. The current standard for this system is the International Temperature Scale 1990 (ITS-90) [1]. The process of temperature measurement typically involves recording temperature quantities measured using thermometers with a record of the measurement conditions. These are generally documented in the process of a ‘calibration’. All devices used for measurements must have an associated uncertainty for each measurement.

1.2 Measurement Error and Uncertainty

The error of a temperature measurement is a quantity that describes the difference between the reading of the measurement thermometer, often referred to as the Unit Under Test (UUT), and the temperature of a standard thermometer. Standard thermometers have a well-defined uncertainty profile which accounts for uncontrolled discrepancies between their reading and the true temperature of the environment.

The uncertainty of a measurement is a measure of the spread of possible values a measurement represents [2]. Lower uncertainties are preferable as they allow for more precision in the measurement process. Achieving lower measurement uncertainties typically requires higher cost equipment and increasingly complex calibration procedure. Higher uncertainty in thermometers can be caused by imperfections in the measuring equipment (electric noise, self-heating) or in the measurement environment (radiation, temperature gradients), as discussed in Section 1.3. Naturally, a UUT will ‘inherit’ the uncertainties of the standard thermometer used to calibrate it, and so it is clearly advantageous to reduce uncertainty as much as practically possible.

An Uncertainty Budget is generally used to record and analyse the collective uncertainties associated with a measurement device and its measurements, and are then referenced during a calibration procedure. The budget provides the values and characteristics of each uncertainty value, as outlined in Section 2.2.

1.3 Platinum Resistance Thermometers

Resistance thermometry is a method of measuring temperature using the property of resistance in a conductor. Platinum is chosen as the conducting metal for many metrology purposes due to its chemical stability and measurement repeatability. It has a well-defined temperature-resistance relationship and a close approximation to Ohm's Law is used to determine the instruments behaviour [3]. Standard platinum resistance thermometers (SPRTs) are generally favoured over alternatives such as thermocouples for calibrations due to their better stability.

A disadvantage of SPRTs is the 'self-heating' effect. When current passes through the platinum sensor, heat is produced according to Joule's Law. This heat increases the thermometers temperature relative to the medium it is submersed in, resulting in a temperature reading error. For this reason, a low current of typically 1 mA is used to minimise heating, but the uncertainty due to self-heating must be quantified and considered.



Figure 1: A glass SPRT with 405 mm probe length. The platinum wire is generally near the tip of the stem.

Smaller platinum resistance probes can be used when a large SPRT cannot be used, such as in a smaller enclosed environment. These are known as 'capsule' probes due to their capsule-like shape. They have a lower mass when compared to larger SPRTs, leading to a more significant self-heating effect.



Figure 2: A capsule probe with 40 mm probe length.

1.4 Air Temperature Metrology

Achieving high accuracy air temperature measurements continues to be a challenge, due to the difficulty in quantifying radiative errors. Many factors contribute to these radiative errors including uncertainty in sensor surface emissivity and difficult to control environmental conditions. Many of these errors have been highlighted by Daniels in 1968 [4], and are still overlooked or insufficiently dealt with recently, as shown by De Podesta *et al* recently [5]. Radiative errors vary depending on many factors including intensity and spectral range of lighting in the measurement environment, sensor diameter and emissivity, as well as the velocity of air and temperature gradients in the environment. De Podesta has discussed the benefits of using non-contact temperature measurements, which use acoustics or laser interferometry to measure temperature [6]. As technology for these devices improves, calibrations will likely require the preparation of air with low uncertainty temperature conditions.

1.5 Project Aims

The aim of this project is to explore an analytical model of air flow past a sensor for the temperature range of $-100\text{ }^{\circ}\text{C}$ to $+100\text{ }^{\circ}\text{C}$. The various behaviours of this system are presented and areas where errors may occur are highlighted. This information may be considered in the production of standard air thermometers and calibration environments such as climatic chambers, and the proposed torus discussed in this project.

The National Metrology Laboratory (NML) have developed a toroidal tube which

can be submerged in a liquid stability bath to control the temperature of the contained air. The viability of this ‘torus’ system will be investigated theoretically, and some preliminary design and experimental work has been carried out. However, due to COVID-19 restrictions, the remaining experimental work is postponed.

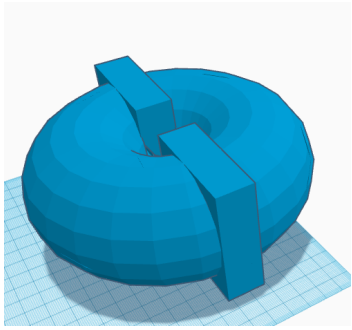
The torus harnesses the capability of the liquid calibration baths which are already available in most temperature metrological settings. Thus, this system may offer an inexpensive alternative to climatic chambers, or provide a method of expanding the temperature range available for air temperature calibrations. With this torus design, the temperature of the walls surrounding the sensor can be controlled with milliKelvin accuracy, and the airflow past the sensors can be known with appreciable accuracy using an anemometer.

The potential reduction of uncertainties due to these advantages will also be investigated. The need for accurate air temperature measurements has been brought to attention recently with the required storage of COVID-19 vaccines at temperatures as low as $-80\text{ }^{\circ}\text{C}$. In addition, the advancement of quantum computing technologies may require precise evaluation of gas temperatures during operation to ensure quantum states are maintained. This project focuses on air temperature measurement, but may be applied to more conductive gases such as helium, often considered for nuclear reactor designs [7].

2 Theory and Background

2.1 Air Temperature Calibration Environment

In most metrological settings, climatic chambers are used as the calibration environment [8]. These machines consist of a volume of air that is sealed in an oven-like machine that regulates the temperature of the air using heaters and refrigerants. Commercially available climatic chambers typically have a temperature range of around $-70\text{ }^{\circ}\text{C}$ up to a few hundred degrees Celsius. However, these systems can cost tens of thousands of euros. The torus consists of two semi-circular tubes made from stainless steel which can be joined using screws to create a sealed volume of air. Gaskets are used to ensure the external liquid does not enter the torus. Three vertical tubes are used as ‘ports’ for inserting sensor wires and powering the fan, as shown in Figure 3.



(a) A 3D model of the torus shape.



(b) The torus with internal fan powered through the 4 mm diameter port on the left and two 10 mm diameter ports on the right are used to insert probes.



(c) The disassembled torus with two white gaskets and fan.

Figure 3: The torus is used to submerge a volume of air in liquid at constant temperature.

The internal fan ensures better thermal coupling of the sensor to the air, and of the air to the torus walls by promoting increased convective heat transfer between surfaces and the air [9]. The 10 mm ports are around 400 mm tall, and the 4 mm port can be extended as needed. This allows the torus to be submerged at optimal immersion depths in liquid stability baths. These baths contain liquid that is maintained at stabilities of typically 1.2 mK over the course of a calibration measurement.

2.2 Uncertainty Budgets

An uncertainty budget is used to calculate the collective uncertainty associated with measurements obtained during an air temperature calibration.

Table 1: A sample uncertainty budget for an air temperature calibration at 173.15 K, which is used for calibrations carried out in a climatic chamber. The values for the temperature stability and homogeneity are omitted, but typically lead to an expanded uncertainty on the order of 0.1 K. An uncertainty budget for 373.15 K is available in Appendix B.

Symbol	Source of uncertainty	Unit	Value ±	Probability Distribution	Divisor	c_i	U_i
U_C	Calibration Uncertainty of Ref. PRT	mK	5	Normal	2	1	2.5
U_{Drift}	Ref. PRT Drift	mK	29	Rectangular	$\sqrt{3}$	1	16.7
U_{RB}	Resistance Bridge Uncertainty	mK	6	Rectangular	$\sqrt{3}$	1	3.5
U_{Axid}	Probe Axial Inhomogeneity	mK	0	Rectangular	$\sqrt{3}$	1	0.0
U_{SH}	Self heating effect	mK	12	Rectangular	$\sqrt{3}$	1	6.9
U_{BS}	Temp. stability	mK	0	Rectangular	$\sqrt{3}$	1	0.0
U_{Hys}	Hysteresis effect	mK	22	Rectangular	$\sqrt{3}$	1	12.7
U_{Rad}	Radiation effect	mK	23	Rectangular	$\sqrt{3}$	1	13.1
U_C	Combined Uncertainty			Normal			26.1
U	Expanded Uncertainty			Normal k=2			0.052 K

The uncertainties due to temperature stability, axial inhomogeneity and radiation can vary depending on the quality of the measurement environment. Typically, these are the primary source of uncertainty, and tend to be around 70 mK for climatic chambers, giving an expanded or total uncertainty on the order of 0.1 K. The uncertainties due to the probe and resistance bridge, including self-heating and hysteresis effects, are due to the design of the measurement equipment and cannot be improved by modifying the measurement environment. The proposed model in this project can be used to inform all other values on the uncertainty budget.

2.3 Thermodynamic Model Overview

A simplified model of the thermodynamic interaction of the sensor has been developed by De Podesta et al. [5]. This model assumes that a temperature sensor is fully immersed in transverse, laminar air flow. The following derivation is carried out for a cylindrical and opaque sensor of length L and diameter D .

Heating of the sensor in the environment occurs due to self-heating and irradiation. The self-heating rate \dot{Q}_{SH} , is:

$$\frac{d}{dt}Q_{SH} = \dot{Q}_{SH} = I^2R(T) \quad (\text{Eqn.1})$$

where the measurement current I for an SPRT is 1 mA, and the resistance R varies approximately linearly with temperature, with a value of 25.5Ω at 0.01°C for most SPRTs and 100Ω at 0.01°C for most industrial PRT sensors. Direct irradiation heating rate is given as:

$$\frac{d}{dt}Q_{Direct} = \dot{Q}_{Direct} = \epsilon_S LDE \quad (\text{Eqn.2})$$

where E is the irradiance in watts per square metre. It is assumed that the angular emissivity and varying spectral response of light-incident surfaces can be approximated by a total hemispherical emissivity ϵ_S . This assumption is based on the fact that the angular emissivity uncertainty is large and so the total of both uncertainties is included in the term ϵ_S . A more detailed analysis of this term is not possible within the context of this work.

From the Stefan-Boltzmann Law, the net radiative flux through the probe, $\dot{Q}_{Radiant}$, is:

$$\frac{d}{dt}Q_{Radiant} = \dot{Q}_{Radiant} = \epsilon_S \sigma A (T_W^4 - T_S^4) \quad (\text{Eqn.3})$$

where σ is the Stefan Boltzmann constant, A is the total probe surface area, T_W is the wall temperature and T_S is the sensor temperature. The flux is negative if the sensor temperature is greater than the wall temperature.

In their book ‘Heat and Mass Transfer’, Çengal and Ghajar [9] provide an equation for the heat transfer between a probe and air due to external forced convection:

$$\frac{d}{dt}Q_{Flow} = \dot{Q}_{Flow} = hA(T_S - T_A) \quad (\text{Eqn.4})$$

where h is the heat transfer coefficient and T_A is the air temperature. For the sensor, air flowing perpendicular to a cylinder at speed V results in a value of h given by:

$$h = \frac{k}{D} Nu_{Cyl} \quad (\text{Eqn.5})$$

where k is the thermal conductivity of air and Nu_{Cyl} is the Nusselt number for a cylinder in a transverse air flow. The same equation can be used to describe airflow

past the torus walls. For the flow past the sensor, the Nusselt number is a dimensionless quantity which describes the approximate relationship of the convective heat transfer to the conductive heat transfer in a gas. The relationship is very complex and a fully analytical theory of the air-cylinder flow behaviour has not been developed. Therefore, the following correlation is recommended in ‘Heat and Mass Transfer’ for the value Nu_{Cyl} :

$$Nu_{Cyl} = 0.3 + \frac{0.62Re^{\frac{1}{2}}Pr^{\frac{1}{3}}}{\left[1 + \left(\frac{0.4}{Pr}\right)^{\frac{2}{3}}\right]^{\frac{1}{4}}} \left[1 + \left(\frac{Re}{282000}\right)^{\frac{5}{8}}\right]^{\frac{4}{5}} \quad (\text{Eqn.6})$$

where Re is the Reynold’s number given by the dimensionless quantity:

$$Re = \frac{\rho V D}{\mu} = \frac{V D}{\nu} \quad (\text{Eqn.7})$$

where ρ is the air density, μ is the dynamic viscosity and ν is the kinematic viscosity. The Prandtl number is given by:

$$Pr = \frac{\nu}{\alpha} = \frac{\mu c_p}{k} \quad (\text{Eqn.8})$$

where α is the thermal diffusivity and c_p is the specific heat capacity. This Nusselt number relation is stated to have a 30% uncertainty and is valid when the product of Re and Pr is greater than 0.2.

At steady state conditions, the sum of the heating rate equations must equal zero. Thus, the heat losses from the probe due to radiation and air heat transfer must equal the heat gained by self-heating and direct irradiation:

$$\dot{Q}_{Flow} = \dot{Q}_{SH} + \dot{Q}_{Direct} + \dot{Q}_{Radian} \quad (\text{Eqn.9})$$

$$hA(T_S - T_A) = I^2R + \epsilon_S LDE + \epsilon_S \sigma A(T_W^4 - T_S^4) \quad (\text{Eqn.10})$$

During operation, the torus is fully sealed and so the value of E will be zero. The direct irradiation term vanishes as a consequence. As $h = \frac{k}{D} Nu_{Cyl}$ and $A = \pi D L$,

$$\Delta T = T_S - T_A = \frac{1}{\pi L k Nu_{Cyl}} [I^2 R + \epsilon_S \sigma A (T_W^4 - T_S^4)] \quad (\text{Eqn.11})$$

The value $T_S - T_A$ is the error of the temperature reading of the sensor. The radiative terms can be approximated by algebraic manipulation [5] as :

$$\epsilon_S \sigma A (T_W^4 - T_S^4) \approx 4\epsilon_S \sigma A T_W^3 \delta T \left(1 + \frac{3}{2} \frac{\delta T}{T_W} + \frac{\delta T^2}{T_W^2} + \frac{\delta T^3}{T_W^3}\right) \quad (\text{Eqn.12})$$

where δT is the difference between the quantities T_W and T_S , not to be confused with ΔT . Omitting the δT terms in the parentheses will produce an error of less than 1% for the expected conditions within the torus and allows for a simplified algebraic solution of T_S :

$$T_S = \frac{I^2 R + 4\sigma\epsilon_S A T_W^4 + hAT_A}{(hA + 4\sigma\epsilon_S A T_W^3)} \quad (\text{Eqn.13})$$

By subtracting T_A from this quantity, the temperature error ΔT is obtained. While the error due to the algebraic approximation is low, solving the fourth order polynomial in T_S removes the need to account for this extra error. This will be carried out using polynomial solvers, which have been implemented in Python using Numpy:

$$\epsilon_S \sigma A T_S^4 + hAT_S - (hAT_A + I^2 R + \epsilon_S \sigma A T_W^4) = 0 \quad (\text{Eqn.14})$$

In previous papers [5] [10], the thermophysical properties of air were assumed constant. In this work, the temperature range of -100 °C to $+100$ °C is investigated, and so the variation of these properties will be considered. Such constant values will be approximated as temperature dependent functions, as discussed in Section 3.

Heat transfer between the sensor and the supports holding the sensor during a measurement can occur if a temperature difference ($T_1 - T_2$) exists between them, causing an error in the sensor reading. The magnitude of this heat transfer is affected by the sensor and support thermal conductivities, and the cross sectional area (A) and length (L) of the supports:

$$\dot{Q} = kA \frac{T_1 - T_2}{L} \quad (\text{Eqn.15})$$

where k is the thermal conductivity of the support material. A measure of the average k value of the support and sensor materials may be needed to model this interaction accurately. To ensure this source of error is minimised, contact between the sensor probe and torus will need to be minimised, and insulation used to reduce the effective value of k .

2.4 Resistance Function Approximation

The resistance value is a function of the sensor temperature, $R(T_S)$. The resistance function used for all calculations is:

$$R(T) = 0.3961205T - 8.2911116 \quad (\text{Eqn.16})$$

which has been determined by using least-squares regression for temperature-resistance data pairs obtained during the course of the sensor calibration. As the value of T_S must be calculated using a resistance value, determining any value of $R(T_S)$ programmatically, will lead to a recursive loop. Thus, the value of $R(T_A)$ will be used for these model calculations. This approximation is used because the difference between T_A and T_W is assumed to be less than 1 °C at all times in the torus. The resulting $|T_S - T_A|$ values, shown in Section 3, tend to be much smaller than this. However, assuming that $|T_S - T_A| = 1$ °C, the percentage difference in the value of R , evaluated at 173.15 K and 174.15 K is around half a percent. This error can be accounted for thoroughly by measuring the sensor resistance at two different currents and applying a correction based on the difference of the two resistances measured [11]. This produces a theoretically ‘zero’ current resistance value.

3 Analysis of the Theoretical Model

This section will focus on developing a more advanced model that accounts for the variation of air properties with temperature. The model developed by De Podesta is expanded upon in this work to produce a semi-empirical model of the complex fluid dynamical interaction between the sensor and the air. A CPU fan is used to blow air around the torus and past the sensors, as the torus diameter of 60 mm is the typical width of a CPU fan. A range of parameters are selected to apply this model to the torus.

3.1 Torus Parameter Selection

The governing equation for the thermodynamic interaction of the air with the sensor is given by Eqn.11, as derived in Section 2.3:

$$\Delta T = \frac{1}{\pi L k N u_{Cyl}} [I^2 R + \epsilon_S \sigma A (T_W^4 - T_S^4)]$$

This equation depends on many parameters, and can be simplified for a variety of conditions. This work will focus on a limited range of parameter values, primarily focused on the function of the torus. In the following calculations and Figures, all parameters will remain at their default values unless being varied as the independent variable. As the torus is designed to be submerged in water and methanol, the temperature range possible with these substances in liquid stability baths will be used. This range is $-100\text{ }^{\circ}\text{C}$ to $+100\text{ }^{\circ}\text{C}$, and it will be assumed that the functions used are valid a few degrees above and below this range. The default parameter values used will be $D = 3\text{ mm}$, $V = 1\text{ ms}^{-1}$, $I = 1\text{ mA}$, $L = 40\text{ mm}$ and $\epsilon_S = 1$.

3.2 Thermophysical Property Functional Approximation

In order to account for the variation of the thermophysical properties of air over the required temperature range, experimental data from literature is fitted to appropriate functions. The functions are approximations that are valid only in the temperature range presented. The errors associated with each value are within a 95% confidence interval by convention in metrology. The air is assumed to be dry, as this can be controlled reasonably well using laboratory air conditioning systems.

An ideal gas approximation is used to define a density-temperature function, giving a T^{-1} dependence from:

$$PV = nRT \quad (\text{Eqn.17})$$

where P is the pressure, taken as the standard value of 101325 Pa , V is volume, n is the number of moles of air, R is the ideal gas constant (8.315 J/molK) and T is temperature in K . Using $n = \frac{m}{M}$, where m is the mass in kg and M is the molar mass of air, the function required is given by:

$$\rho(T) = \frac{PM}{RT} = 353.044T^{-1} \quad (\text{Eqn.18})$$

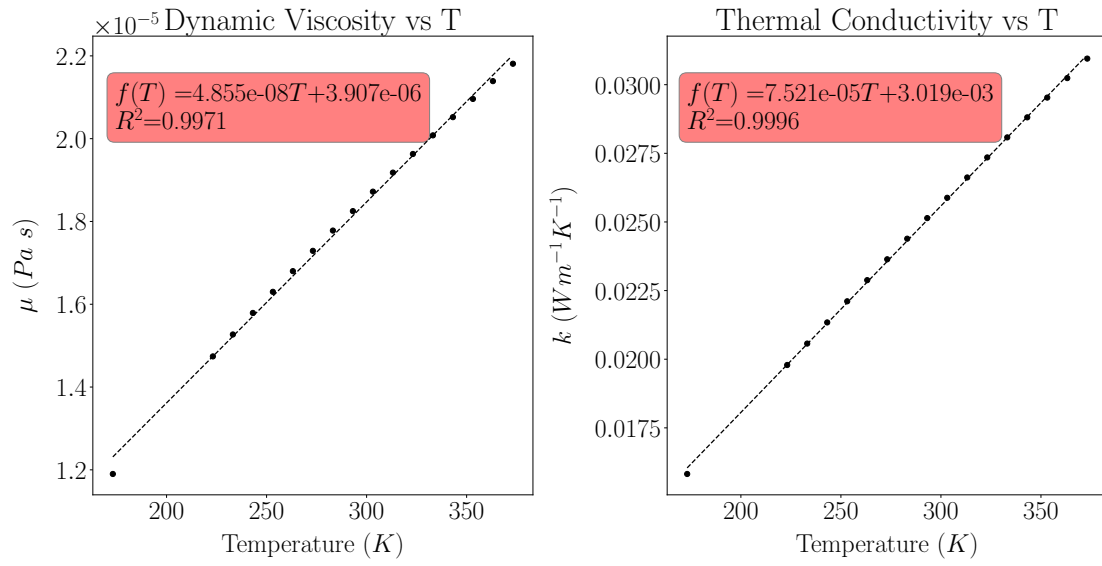


Figure 4: Data for dynamic viscosity and thermal conductivity [9] as a function of temperature.

From Figure 4, the following functions can be used to approximate the dynamic viscosity (μ) and thermal conductivity (k):

$$\mu(T) = (4.855 \pm 0.145) \times 10^{-8} + (3.907 \pm 0.430) \times 10^{-6} \text{ Pa} \cdot \text{s} \quad (\text{Eqn.19})$$

$$k(T) = (7.521 \pm 0.083) \times 10^{-5} + (3.019 \pm 0.246) \times 10^{-3} \text{ W/m} \cdot \text{K} \quad (\text{Eqn.20})$$

The specific heat capacity (c_p) of air varies across the temperature range. The data available over this temperature range [9] can be accurately fitted appropriately using a T^3 function, in line with theoretical models of specific heat capacity. However, as the model is already limited by the uncertainties in Eqn.6 and sensor emissivity ϵ_S , a constant c_p value approximation is chosen as:

$$c_p = 986 \pm 22 \text{ J/kg} \cdot \text{K} \quad (\text{Eqn.21})$$

The kinematic viscosity is given by $\nu = \frac{\mu}{\rho}$, shown in Figure 5:

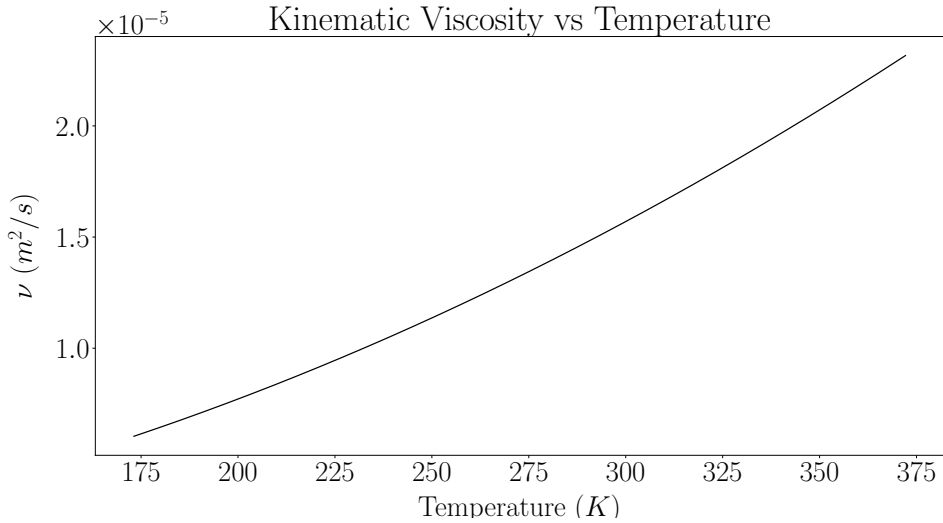


Figure 5: The kinematic viscosity variation across the temperature range.

3.3 Nusselt Number Analysis

The Nusselt number relation in Eqn.6 for flow past a cylinder is complex, but can be simplified to investigate the general behaviour of the function. However, for all code used involving Nu_{Cyl} , the full relation will be used. The upper limit of the Reynold's number required is found by using the values of $D = 9\text{ mm}$, $V = 1\text{ ms}^{-1}$ and $\nu = (2.631 \pm 0.082) \times 10^{-5}\text{ m}^2/\text{s}$ for air at $-100\text{ }^\circ\text{C}$ to give $Re \approx 1700$. This allows the $\frac{4}{5}$ term to be approximated as unity with an error of around 3%.

$$Nu_{Cyl} = 0.3 + \frac{0.62 Re^{\frac{1}{2}} Pr^{\frac{1}{3}}}{\left[1 + \left(\frac{0.4}{Pr}\right)^{\frac{2}{3}}\right]^{\frac{1}{4}}} \quad (\text{Eqn.22})$$

The value of Re varies by a factor of around 4 with temperature while the value of Pr varies by around 10%, as shown in Figure 6.

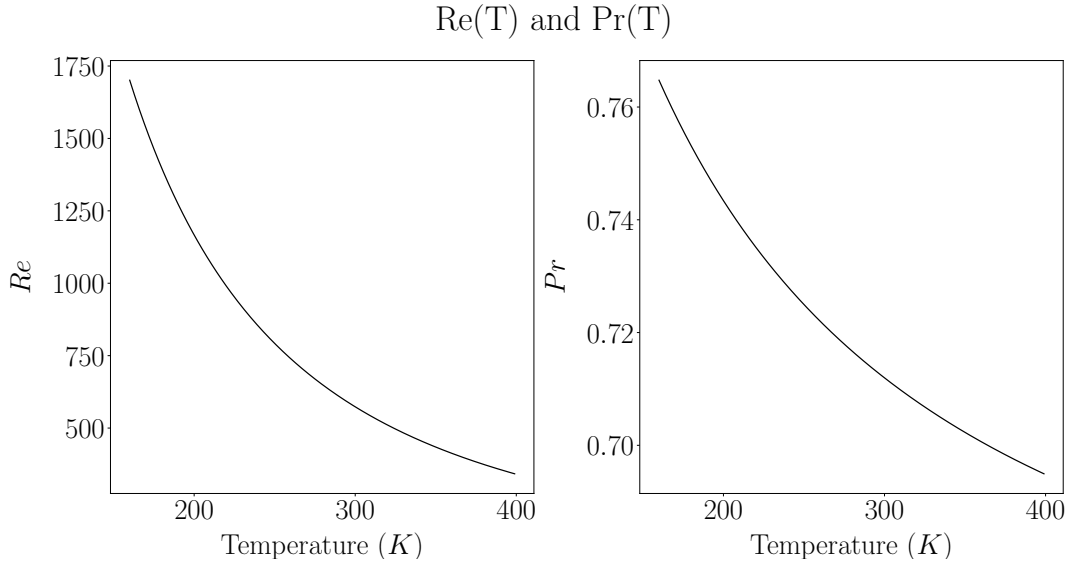


Figure 6: Variation of the Reynold's number Re and Prandtl number Pr over the temperature range. The values for Re are shown for $D = 9\text{mm}$ and $V = 1\text{ms}^{-1}$.

Therefore, the value of Pr can be approximated as a constant:

$$Pr = (0.72 \pm 0.04) \quad (\text{Eqn.23})$$

This approximation only adds an extra uncertainty of around 1% due to the uncertainties of roughly 4% in the quantities used to calculate Pr across the temperature range. With Pr as a constant, the value of Nu_{Cyl} can be shown to be proportional to the square root of the Reynold's number:

$$Nu_{Cyl} \propto Re^{\frac{1}{2}} \propto \left[\frac{VD}{\nu(T)} \right]^{\frac{1}{2}} \quad (\text{Eqn.24})$$

The result shows that the value Nu_{Cyl} should vary proportionally to $V^{\frac{1}{2}}$, $D^{\frac{1}{2}}$ and inversely proportional to $\nu(T)^{\frac{1}{2}}$. Using this Nusselt number simplification, it can be shown that the temperature error varies as:

$$\Delta T \propto \frac{\nu^{\frac{1}{2}}}{LkV^{\frac{1}{2}}D^{\frac{1}{2}}} [I^2 R + 4\epsilon_S \sigma A T_W^3 (T_W - T_S)] \quad (\text{Eqn.25})$$

where the notation $f(T) = f$ has been used for the temperature dependent quantities.

3.4 Diametric Error Dependence

3.4.1 Contrary Square Root Dependences

The ports on the torus for insertion of probes are 10 mm in diameter, so a range of 0.1 mm to 9 mm is chosen. At constant temperature conditions and with ideal torus operation ($T_W = T_A$), Eqn.25 simplifies to:

$$\Delta T \propto \frac{1}{D^{\frac{1}{2}}}$$

As there is no direct illumination of the sensor and the temperature difference between the wall and air is minimal, an inverse square root dependence is observed, as shown in Figure 25. This behaviour occurs when the magnitude of the self-heating term is larger than that of the radiative term. If the radiative term becomes dominant, the area term cancels with the $D^{-\frac{1}{2}}$ term to give:

$$\Delta T \propto D^{\frac{1}{2}}$$

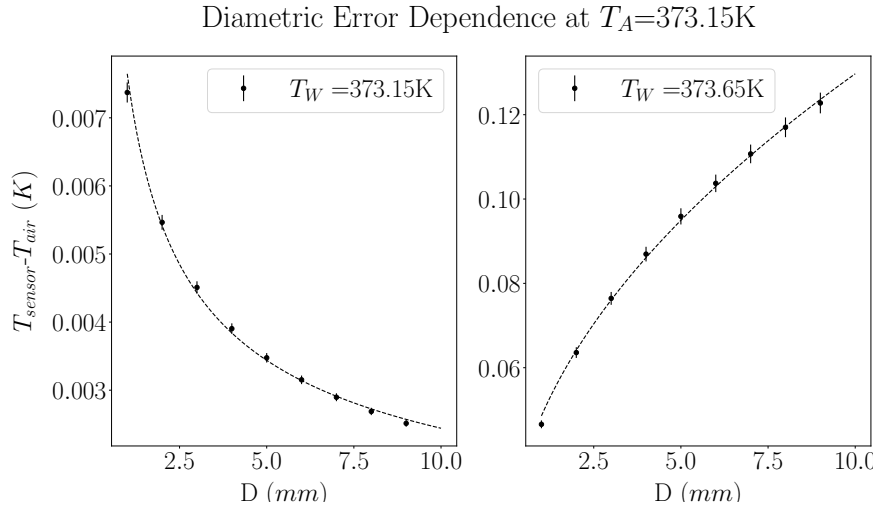


Figure 7: The model diametric error dependence at $T_A = 373.15\text{ K}$, with an expected square root and inverse square root behaviour for the values of T_W shown.

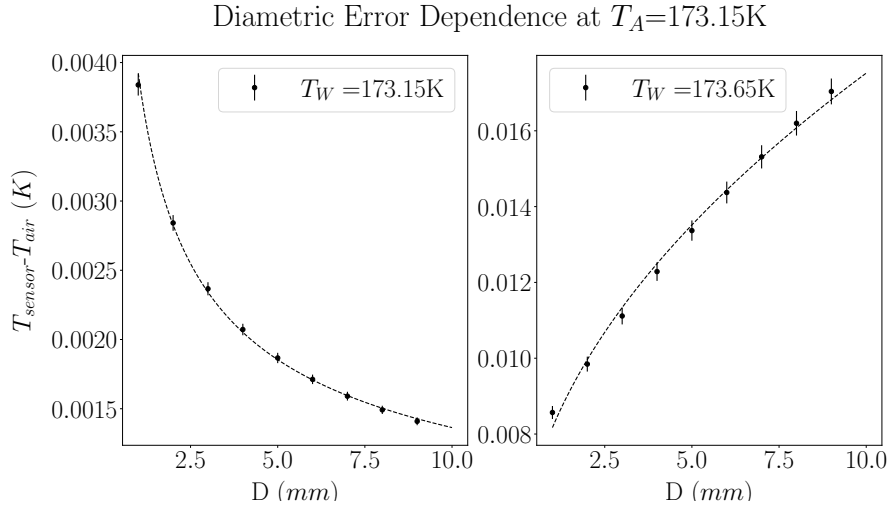


Figure 8: The model diametric error dependence at $T_A = 173.15\text{ K}$, with an expected square root and inverse square root behaviour for the values of T_W shown. The overall error magnitudes are smaller.

The $D^{\frac{1}{2}}$ and contrary $D^{-\frac{1}{2}}$ behaviour, shown in Figures 7 and 8, is an interesting effect as the behaviour of sensor error at one set of temperature conditions can behave in the opposite manner to a set of temperature conditions just a few tenths of a degree different. Under these conditions, using thinner sensors will actually result in larger errors than using large diameters. This is an effect that has not been highlighted in the previously mentioned papers.

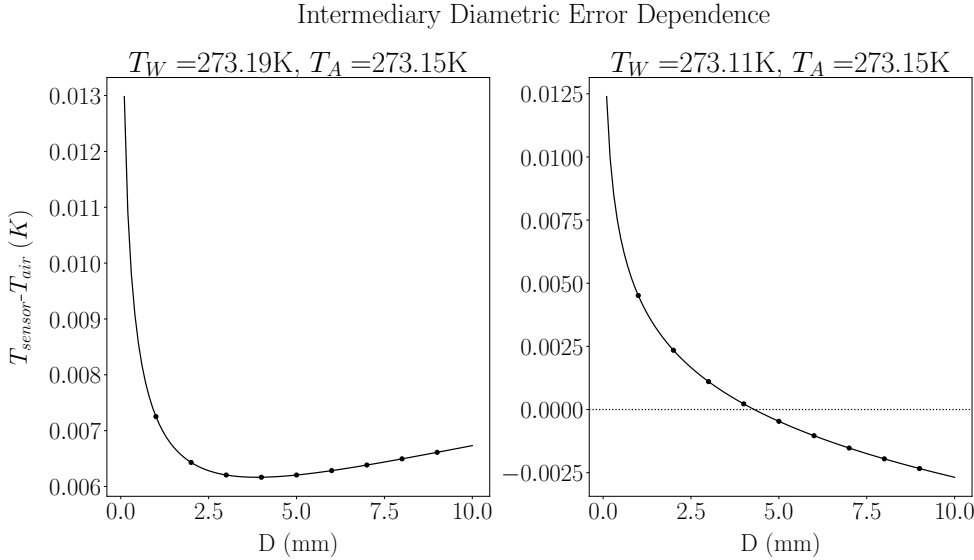


Figure 9: For the given temperature conditions, the error decreases for smaller diameter sensors before increasing as the diameter exceeds around 4 mm. The dotted line highlights where the error begins to increase again.

The diametric inverse square root error dependence becomes a square root dependence when the diameter is increased for particular temperature conditions, due to the larger sensor surface area. For this reason, it is possible for sensors with different diameters to have roughly the same temperature error, shown in Figure 9. This will be referred to as an intermediary diametric error dependence. A *U*-shaped curve occurs for $T_W > T_A$ and an *x*-axis intersection occurs for $T_W < T_A$. The magnitude ratio of the self-heating and radiative terms can be used to understand these conditional behaviours:

$$\frac{|I^2 R|}{|4\sigma\epsilon_S A T_W^3 (T_W - T_S)|} \quad (\text{Eqn.26})$$

In general, the quantity in Eqn.26 must be greater than unity in order for the square root dependency is expected, while if it is less than unity the inverse square root dependency is expected. The value A in this case, represents the range of possible areas the sensor can have. In order to investigate the values of T_A and T_W at which the diametric error dependence changes, the approximation $T_S \approx T_A$ is used.

$$\frac{|I^2 R|}{|4\sigma\epsilon_S A T_W^3|} = |T_W - T_A| \quad (\text{Eqn.27})$$

The error induced by this approximation is the difference in T_S and T_A , the temperature error of the sensor. From the previous results, it is found that the worst case

error of less than 8 mK occurs for a 1 mm diameter sensor at $T_W = T_A = 373.15 \text{ K}$. By solving for the quantity $|T_W - T_A|$ for the range of diameters in question, the conditions at which the square root dependence changes can be given with an error of 8 mK .

3.4.2 Zonal Dependencies

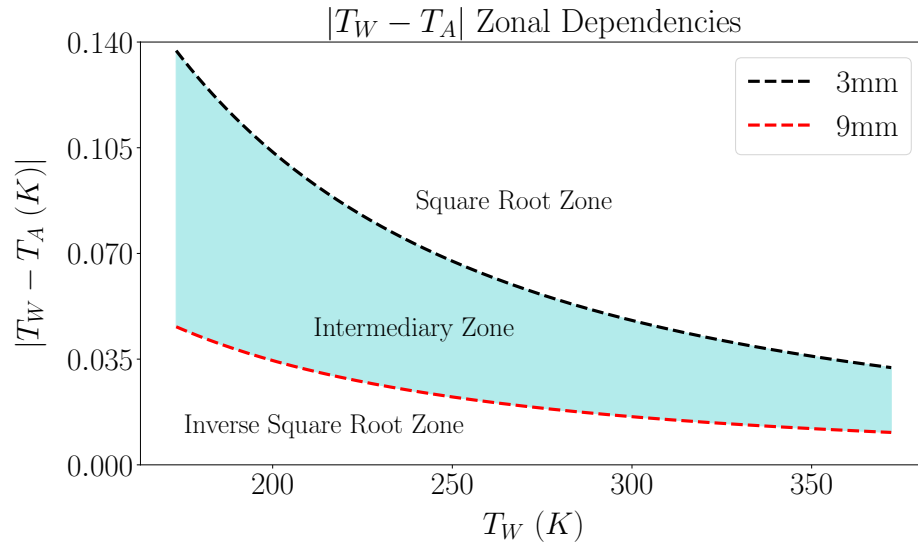


Figure 10: The three zones represent temperature conditions for which the three behaviours of the error-diameter dependency occur. The dotted lines have a T^{-2} best fit.

Figure 10 shows the magnitude of the wall-air temperature difference across the required temperature range, for the diameter range of 3 mm to 9 mm . Any point between the 3 mm curve and the x -axis describes the conditions for which an inverse square root diametric error dependency occurs across the diameter range. Any point above the 9 mm curve describes the conditions for which a square root diametric error dependency occurs. Finally, any point between the 3 mm and 9 mm curves describes the conditions for which an intermediary root diametric error dependency occurs. These temperature conditions are graphically represented as zones above, between and below the dotted curves. The linear temperature dependence of the resistance term and the T_W^3 term in Eqn.26 result in all possible curves scaling by T^{-2} .

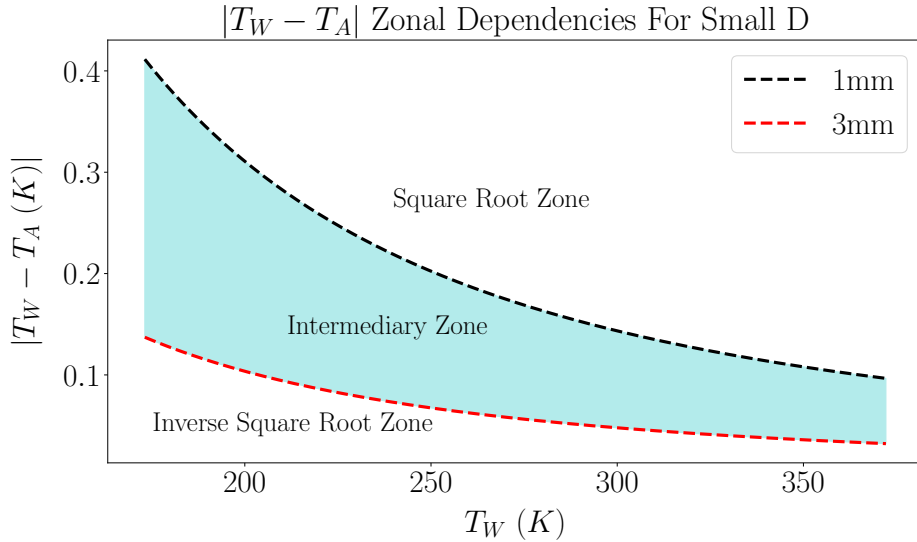


Figure 11: For diameters from 1mm to 3mm, the intermediary and inverse square root zones cover much larger temperature differences.

The exact values that define these curves will depend on the resistance of the sensor, L and D . The value of L has been chosen as the default parameter value of 40 mm for the graphs shown. As the area term in Eqn.26 is proportional to both the length L and diameter D , doubling either of these quantities reduces the value of $|T_S - T_A|$ by a factor of two for any chosen value of T_W . This is an important consideration, as intermediary behaviour is expected for modest values of $|T_W - T_A|$.

3.5 Length Error Dependence

Choosing a sensor with a 3 mm diameter, the length can be varied for a variety of temperature conditions. As the diameter of the torus tube is around 60 mm, the sensor length range of 10 mm to 60 mm will be chosen. The self-heating term will be dominant for small values of $|T_W - T_A|$. At steady-state conditions, the error can be simplified as:

$$\Delta T \propto \frac{1}{L} \quad (\text{Eqn.28})$$

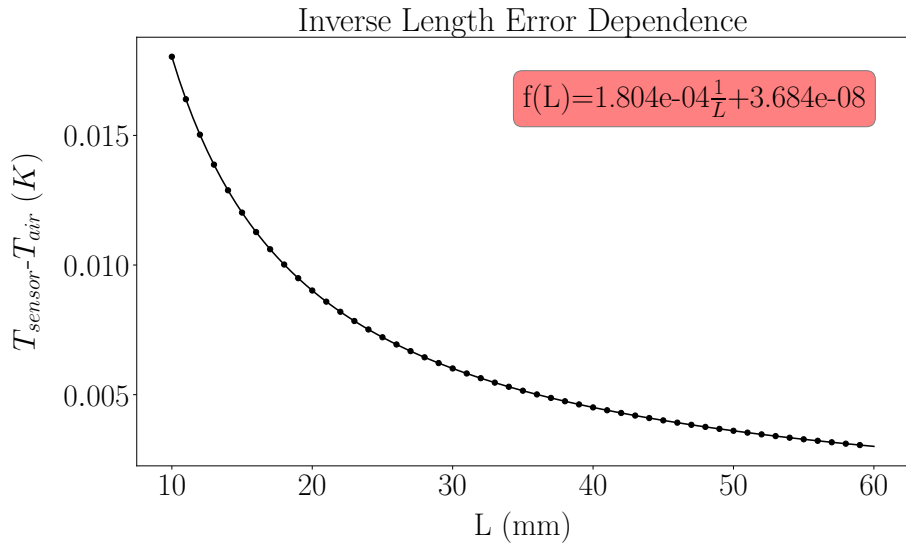


Figure 12: The model shows the sensor error has an inverse length dependence at $+100^{\circ}\text{C}$.

With a dominant radiative term, the temperature error should be approximately independent of the sensor length, as the L terms cancel in Eqn.25. Due to the self-heating term, an inverse error-length dependence will still be present, but with a much smaller significance for the overall error. In Figure 12, the value of the error varies by a factor of roughly three across the length range of 10 mm to 60 mm. As the value of L becomes arbitrarily large, the error approaches $3.7 \times 10^{-8} \text{ K}$, an unmeasurable error for any practical temperature measurement system.

Figure 13 shows the same inverse length behaviour. The ‘inverse proportionality constant’ of 1.8×10^{-4} remains the same. However, for arbitrarily large values of L , the best case error will still be on the order of 0.1 K due to the measurement conditions. Across the length range, a smaller error reduction of around 10% is possible. Therefore, increasing L has a more negligible effect on the temperature error.

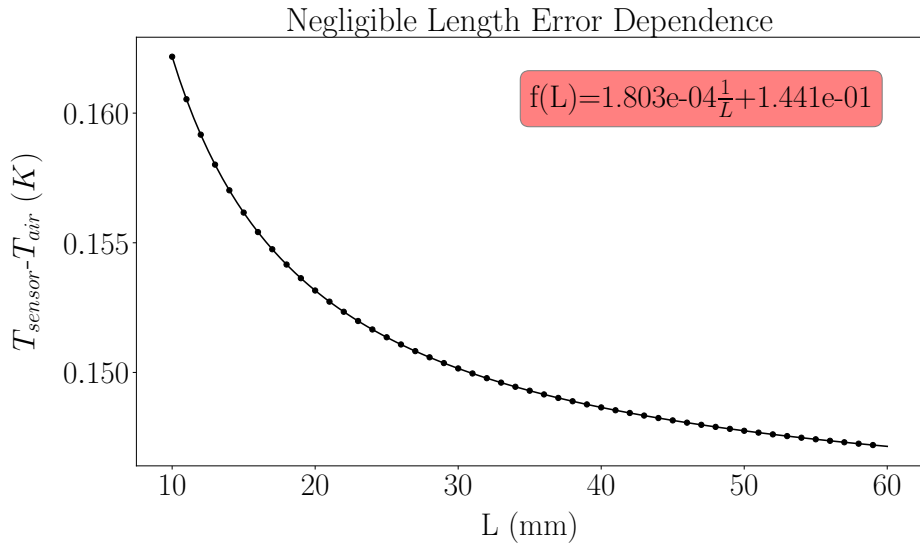


Figure 13: The inverse length dependency with $T_W = 101.000 \text{ } ^\circ\text{C}$ and $T_A = 100.000 \text{ } ^\circ\text{C}$.

3.6 Velocity Error Dependence

The CPU fans with rotational speeds of approximately 5000 RPM produce roughly 1 ms^{-1} flow speeds in the sealed torus. From Eqn.25, an inverse square root dependency is expected for all possible model conditions. The upper limit of the velocity range is chosen as 1 ms^{-1} , as this is the upper limit of the flow rate possible with all tested fans. The lower bound can theoretically be chosen as any non-zero value. However, the Nusselt number correlation used in Eqn.6 is only valid when the product of Re and Pr is greater than 0.2 [9].

$$V > \frac{0.2\nu}{D \cdot Pr} \quad (\text{Eqn.29})$$

Solving Eqn.29 with model parameters that maximise the lower bound air flow velocity, using $D = 1 \text{ mm}$, $Pr = 0.70$ and $\nu(393.15 \text{ K}) = 2.32 \times 10^{-5} \text{ m}^2 \text{s}^{-1}$, the result is calculated as 0.007 ms^{-1} . The resolution of the Testo 425 Thermal Anemometer is 0.01 ms^{-1} so this will be chosen as the lowest velocity for the model.

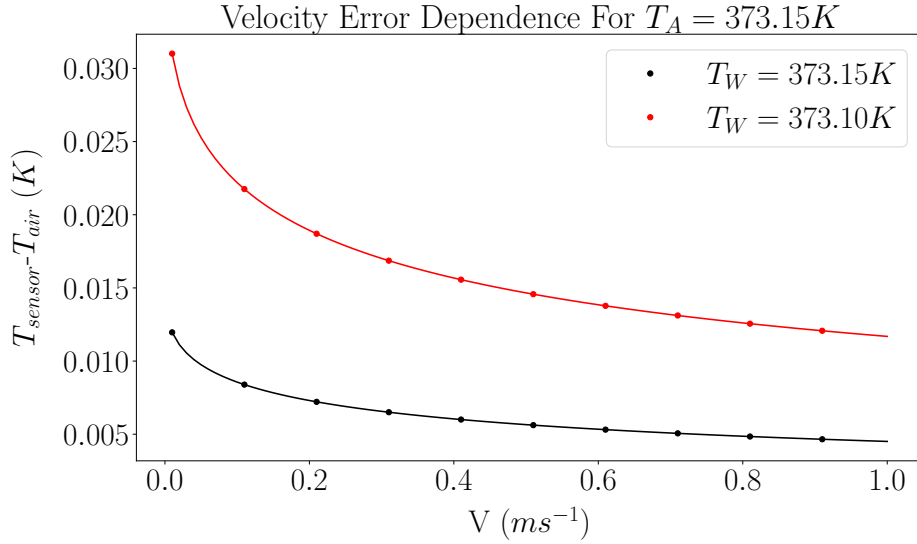


Figure 14: An inverse square root velocity-error dependence is predicted for all possible torus conditions. The values are shown for $D = 3 \text{ mm}$ and $L = 40 \text{ mm}$.

3.7 Temperature Error Variation

In Eqn.25, there are many temperature dependent variables including the kinematic viscosity and conductivity of air, the resistance of the sensor and the temperature quantities T_W and T_A :

$$\Delta T \propto \frac{\nu^{\frac{1}{2}}(T)}{k(T)} [I^2 R(T) + 4\epsilon_S \sigma A T_W^3 (T_W - T_S)] \quad (\text{Eqn.30})$$

The ratio of $\nu^{\frac{1}{2}}(T)$ to $k(T)$ varies by approximately 1%, so the variation of the thermophysical properties of air across the temperature range have only a small effect on the variation of sensor error. By approximating this ratio as a constant, the system behaviour can simplified to:

$$\Delta T \propto 10^{-6} R(T) + 9 \times 10^{-11} T_W^3 (T_W - T_S) \quad (\text{Eqn.31})$$

For $T_A \approx T_W$, the term $T_W - T_S$ will be a negative quantity not exceeding a few milliKelvin, as shown in previous Figures. The magnitude of the linear resistance term will be on the order of 10^{-5} , while the magnitude of the radiative term will be on the order of around 10^{-6} for the lower range temperatures, and 10^{-5} for the higher

range temperatures. For this reason, the resistance term can be assumed to be the dominant term, resulting in a roughly linear increase in temperature error across the temperature range. The negative radiative term will become significant for higher temperature ranges, reducing the rate of increase of error.

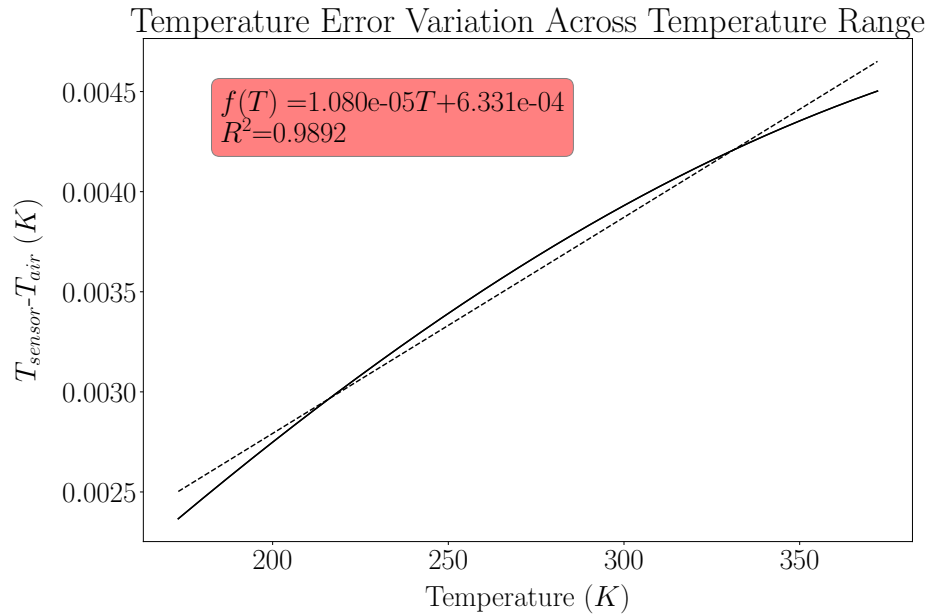


Figure 15: The variation of a 3mm diameter sensor error across the temperature range can be approximated by a linear function for ideal torus conditions ($T_W = T_A$). The dotted fit line is given by $f(T) = (1.080 \pm 0.0158) \times 10^{-5}T + (6.331 \pm 0.440) \times 10^{-5}$.

For non-negligible and constant values of $T_W - T_S$, the radiative term is dominant and so the linear term can be disregarded. It is then expected that the error will vary roughly proportionally to T_W^3 .

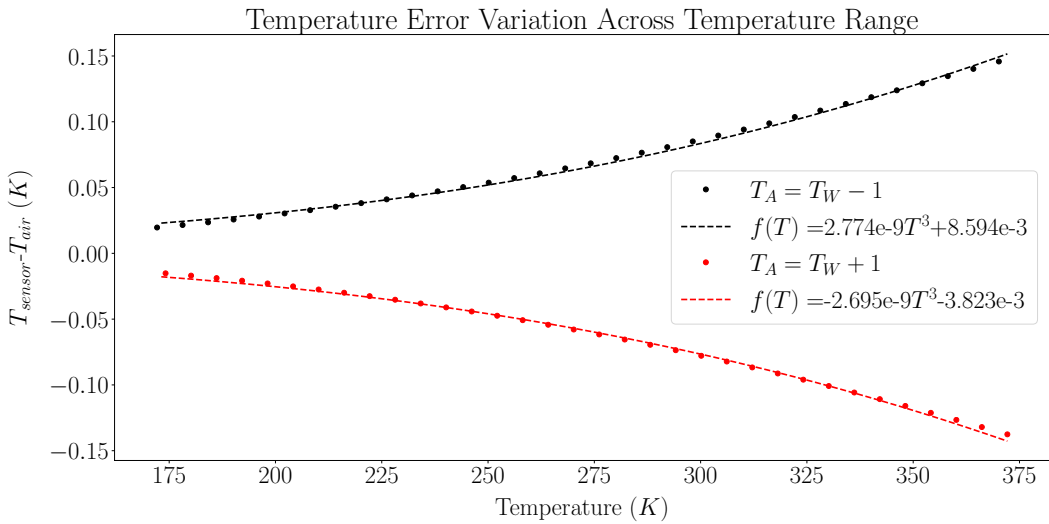


Figure 16: The variation of a 3mm diameter sensor error across the temperature range can be approximated by a cubic function, with an error of around 3% for the fit functions shown.

4 Results and Discussion

4.1 Theoretical Model

An advanced theoretical model that considers thermophysical properties of air has described the expected behaviour of temperature errors across the temperature range required. The model results assume that it is possible to achieve conditions where air temperature stability and homogeneity on the order of a few milliKelvin. While it is possible to achieve this for the value T_W using liquid calibration baths, it is a much greater challenge for T_A , as discussed in Section 4.3.8. For ease of reading, ‘ideal’ torus conditions will refer to conditions where negligible radiative heat transfer at the sensor walls occur. This is achieved at small values of ($|T_W - T_A|$). ‘Unideal’ torus conditions will refer to conditions where non-negligible radiative heat transfer occurs at larger ($|T_W - T_A|$) values.

The variation of the sensor error with diameter is very significant and must be accounted for in order to minimise the total error. A square root diametric error dependence is predicted for conditions where the magnitude of the wall-air temperature difference ($|T_W - T_A|$) exceeds the values predicted by the inverse T^2 curve shown in

Figures 10 and 11. The exact values of these curves will vary depending on the sensor resistances and surface areas. For temperature conditions described by values of $|T_W - T_A|$ above this curve, the following correction formula can be used to determine the air temperature using the ratio of two points with a square root dependency can be used (provided by De Podesta [5] *et al*):

$$T_A = \frac{T_1 - T_2 \left(\frac{D_1}{D_2} \right)^{\frac{1}{2}}}{1 - \left(\frac{D_1}{D_2} \right)^{\frac{1}{2}}} \quad (\text{Eqn.32})$$

However, there seems to an inaccuracy in Equation 15 from their paper [5] which is:

$$(T_S - T_A) \propto \dot{Q}_{\text{Flow}} \left(\frac{D}{V} \right)^{\frac{1}{2}}$$

Deriving this statement is not possible when beginning from Eqn.4. Instead, one arrives at a $D^{-\frac{1}{2}}$ dependence, as discussed in Section 3. To reconcile this, the \dot{Q}_{Flow} term in their equation may be more thoroughly represented a collective term including the radiative terms. These terms have a factor of D which results in the $D^{\frac{1}{2}}$ dependence (see Appendix B). Thus, considering negligible radiative effects, the temperature error is inversely proportional to the diameter. These conditions are described by points below the inverse T^2 curves, where a modified equation can be used to determine air temperature:

$$T_A = \frac{T_1 - T_2 \left(\frac{D_1}{D_2} \right)^{-\frac{1}{2}}}{1 - \left(\frac{D_1}{D_2} \right)^{-\frac{1}{2}}} = \frac{T_1 - T_2 \left(\frac{D_2}{D_1} \right)^{\frac{1}{2}}}{1 - \left(\frac{D_2}{D_1} \right)^{\frac{1}{2}}} \quad (\text{Eqn.33})$$

Figures 10 and 11 show that this inverse square root error-diameter dependence is expected for ideal torus conditions. In these circumstances, using thicker sensors is favourable for lower error calibrations. For conditions where the intermediary behaviour is observed, these formulae will not be valid. This is achieved by minimising air heating from the fan to produce ideal torus conditions. If the fan heating rate results in conditions within the square root zone, it is possible to accurately determine the air temperature using Eqn.32 provided the air temperature remains stable. Using larger diameter sensors will result in lower response times due to the increased thermal mass of the probe. During a calibration procedure, this will increase the time required for stabilisation to occur. Research in this area has been carried out in 2020 by Burton

and De Podesta [12]. They quantify a measure of this temperature lag as a response time τ :

$$\tau \propto \frac{D^{1.5}}{\sqrt{V}} \quad (\text{Eqn.34})$$

This equation may be useful to consider along with the previous information once the torus performance has been profiled.

Capsule probes, shown in Figure 2, are a suitable type of sensor, as they are around 40 mm in length and have diameters in the range required for the torus. The model assumes that the probes are fully submerged in the air flow. If the sensor length exceeds the diameter of the torus tube, a portion of the sensor will remain in the port. Air flow in these regions is expected to be much lower given that the torus is sealed. For this reason, it may be necessary to carry out further investigations into stem conduction effects with physical experiments.

The model predicts that errors will be reduced at a rate inversely proportional to the sensor length. It is favourable to use longer sensors for this reason. The appropriate sensor length should be chosen to prevent contact between the torus walls and the sensor. For increasingly unideal torus conditions, the percentage reduction of the error by increasing the sensor length will decrease.

The model also predicts that for all possible torus conditions, there will be an inverse square root error-velocity relationship. This relationship has been verified experimentally [13]. The priority in the experimental work of this project has been to maximise air flow in order to maximally reduce sensor error. This has led to excessive heat output by the fan, as discussed in Section 4.3.3. The heating rate of the fan is likely to increase as more work is done to spin the fan, and this is shown in Figure 22. Therefore, it may be advantageous to use lower air speeds if a significant reduction of fan heating is achieved. Due to the motion of the fan blades, the air within the torus is likely to be turbulent due to the non-uniformity of the air velocity around the fan fins. As this model is based on laminar flow, the flowing air may need to be corrected using a honeycomb flow straightener used in previous works [10]. However, increasing turbulence will lead to larger heat transfer coefficients due to increased thermal mixing [9]. Utilising this turbulence may be advantageous in reducing sensor error.

The variation of error across the temperature range is very reasonably described by the linear and cubic approximations in Section 3.7. This is an important consideration as an identical experimental set up will not produce the same quality of temperature measurement at higher temperatures when compared to lower ones. The variation of error across the temperature range is primarily due to T_W^3 term, which is much more dominant compared to the thermophysical properties.

As uncertainty budgets generally describe uncertainties at temperature range intervals, this model result is very useful in aiding the compilation of uncertainty budgets. Theoretical uncertainty budgets have been compiled in this project, and are available in Section 2.2.

4.2 CFD Results

Typically, CFD simulations are validated using experimental data. Under the constraints of this project, ANSYS® Fluent has been selected to provide CFD simulations in place of experimental results. The theoretical model developed in Section 3 utilises new analytical equations and new and existing semi-empirical correlations. The results obtained from CFD simulations are based on partial differential equations like the Navier-Stokes equations, which are solved using numerical methods. It is proposed that the unique mathematical basis of both of these methods provides an appreciable indication that the model will apply to physical experiments. The sensor surface heat flux data is the only direct information that has been transferred from the theoretical model to the CFD software in order to reduce bias as much as possible.

4.2.1 Simulation 3D Model

A 3D model of six cylinders with varying diameters are modelled using ANSYS®. Each cylinder has a length of 40mm, and these are separated by 25 mm as shown in Figure 17. These are surrounded by a large cylinder through which air flow passes in order to replicate the torus walls. ANSYS® uses the finite volume method (FVM) [14] to solve the Navier-Stokes equations that govern fluid flow. To achieve this, the 3D model is discretised into polygonal cells, called a mesh. For these results, 502,868 cells were used which is very close to the limit of what is achievable with the student version of ANSYS®. The mesh was refined around the cylinders to improve the accuracy of the model results. By using the maximum amount of elements,

the errors caused by the FVM approximations are typically minimised as much as possible. The student software also means there is a limitation on the number of CPU processors available for the simulation. For these reasons, it is assumed that any errors produced by the discretisation approximations are negligible. The results are obtained by a process which averages the values of various physical properties of adjacent cells to produce resultant values. The simulation process also tracks the values expected by the Law of Conservation of Energy and the associated errors due to the discretisation approximations. These are kept within a tolerance known as the ‘convergence criteria’.

A 3D model was chosen over a computationally less expensive 2D model in order to most accurately capture the radiation effects between all surfaces.

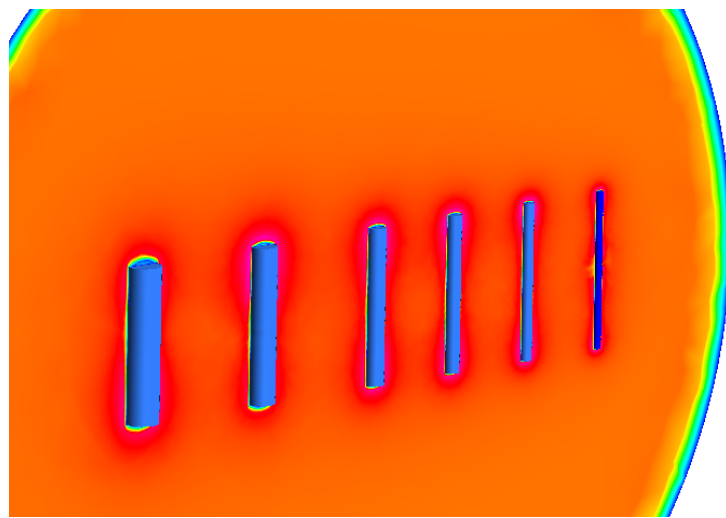


Figure 17: The geometry used in the CFD simulation. The sensors are placed 25 mm apart to reduce radiation effects between sensors.

4.2.2 Ansys® Model Settings

The model settings have been chosen based on the recommendations from the ANSYS® documentation [15]. The ANSYS® Fluent steady-state pressure-based solver was used. Gravity is assumed to have a negligible effect on the properties of the air. The laminar flow model was selected with the viscous heating option enabled in an attempt to capture any subtle viscosity effects near the sensor surfaces. For radiation effects, the surface-to-surface (S2S) radiation model was selected with the default parameters. This radiation model is appropriate for optically thin media such as air, in this case

[16].

The thermophysical properties of air are approximated using the Aungier-Redlich-Kwong (ARK) real gas model in an attempt to account for subtle effects not captured with an ideal gas model. The various parameters of this real-gas option are left at the default values. This ARK approximation is assumed to be appropriate as it reasonably describes fluids where no liquid is present, as expected in the torus. All other properties of air are approximated with the ‘kinetic theory’ option to account for thermophysical property variation with temperature. The surrounding tube material is chosen as 3 mm thick steel and the cylinder material is 1 mm thick Inconel, as this is used as the SPRT sheath material for many probes. The inlet air velocity is 1 ms^{-1} and the outlet pressure is zero Pascals. The torus wall and air temperature were varied to obtain the required results.

The internal and external emissivities for all materials are left at the default value of 1. To replicate the self-heating effect, a surface heat flux must be applied to each of the cylinders. These values are calculated by dividing the $I^2R(T)$ value by the surface area of the sensor:

Table 2: The surface heat rate for each sensor to simulate the self-heating effect is calculated by dividing the $I^2R(T)$ value by the total surface area of the sensors. It is assumed each sensor has the same resistance, calculated using Eqn. 16.

D	Surface Heat Flux (W/m^2)	
	T = 173.15 K	T = 373.15 K
2mm	0.234	0.542
3mm	0.154	0.357
4mm	0.114	0.264
5mm	0.090	0.209
7mm	0.063	0.146
9mm	0.048	0.111

All values for the convergence criteria were set to 10^{-5} . The hybrid initialisation setting is used, and the simulation is run across 450 iterations. All the error values reach this criteria except for the continuity error, which reaches around 10^{-2} . The energy residual reaches 10^{-8} . Under the computational limits of this project, these values are assumed to be sufficiently accurate.

4.2.3 Model Comparison

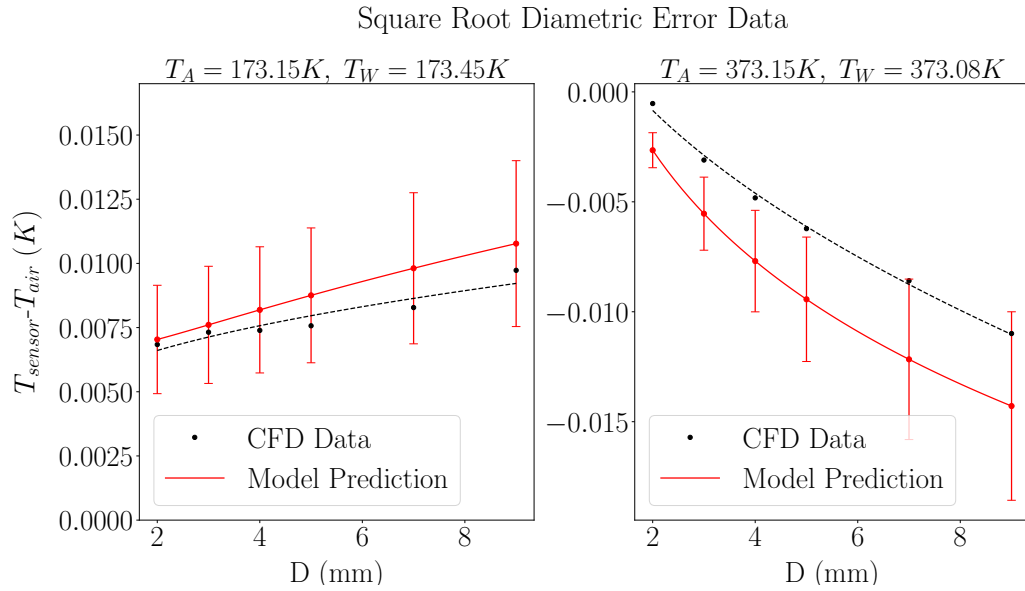


Figure 18: The data obtained for the CFD simulation for unideal torus conditions and the model predictions. The fitted function values are given in Table 3.

Table 3: The data plotted in Figure 18 with good agreement between the model and CFD values. The fit functions are of the form $\Delta T = AD^{\frac{1}{2}} + B$.

	T_W (K)	Offset (K)	$D^{\frac{1}{2}}$ Coefficient ($K \text{ mm}^{-\frac{1}{2}}$)
CFD	173.450	$(4.28 \pm 1.40) \times 10^{-3}$	$(1.65 \pm 0.62) \times 10^{-3}$
Model	173.450	$(3.53 \pm 1.06) \times 10^{-3}$	$(2.38 \pm 0.71) \times 10^{-3}$
CFD	373.080	$(8.24 \pm 0.82) \times 10^{-3}$	$(-6.42 \pm 0.37) \times 10^{-3}$
Model	373.080	$(7.18 \pm 2.15) \times 10^{-3}$	$(-7.28 \pm 2.18) \times 10^{-3}$

The square root dependence has been shown experimentally at room temperatures in [5] and the CFD results in Figure 18 are described very reasonably by this model also. The large error bars are primarily caused by the 30% uncertainty in Nu_{Cyl} .

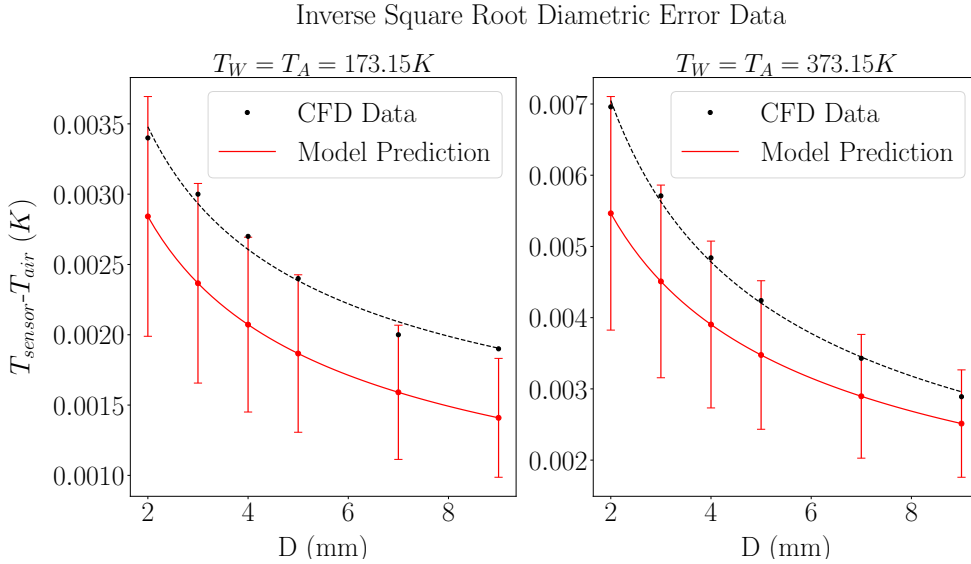


Figure 19: The data obtained for the CFD simulation for ideal torus conditions and the model predictions. There is good agreement between the model and CFD values, shown in Table 4.

Table 4: The data plotted in Figure 19. The $D^{-\frac{1}{2}}$ coefficient is close to agreement with model values (although there is a slight discrepancy in the 373.15 K coefficient). The fit functions are of the form $\Delta T = AD^{-\frac{1}{2}} + B$.

	T_W (K)	Offset (K)	$D^{-\frac{1}{2}}$ Coefficient ($K \text{ mm}^{\frac{1}{2}}$)
CFD	173.150	$(5.00 \pm 2.78) \times 10^{-4}$	$(4.21 \pm 0.55) \times 10^{-3}$
Model	173.150	$(1.84 \pm 0.55) \times 10^{-3}$	$(3.82 \pm 1.05) \times 10^{-3}$
CFD	373.150	$(-6.87 \pm 2.56) \times 10^{-4}$	$(1.09 \pm 0.05) \times 10^{-2}$
Model	373.150	$(-8.23 \pm 2.47) \times 10^{-5}$	$(7.90 \pm 2.37) \times 10^{-3}$

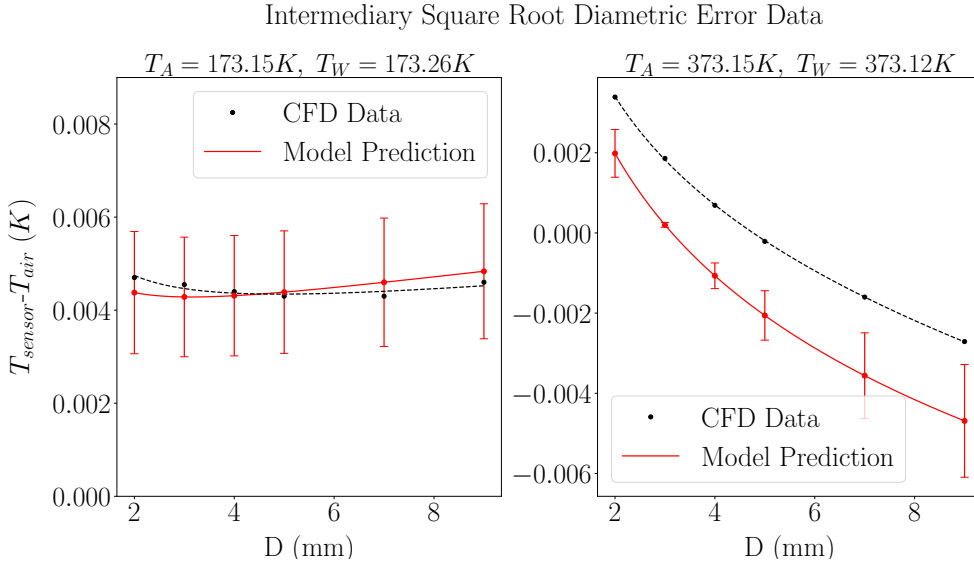


Figure 20: The data obtained for the CFD simulation for conditions leading to intermediary behaviour. Values plotted from Table 5.

The CFD data in Figures 19 and 20 are in considerable agreement with the model values. The ideal torus conditions are described quite accurately by an inverse square root dependence, and intermediary behaviour occurs as expected qualitatively, with U-shaped behaviour shown for the conditions at $-100\text{ }^{\circ}\text{C}$ with $T_W > T_A$ and x -axis intersection for conditions at $+100\text{ }^{\circ}\text{C}$ with $T_A > T_W$. There is a discrepancy between the predicted diameter which produces the smallest error. However, the results are still within 1 mK of accuracy. All uncertainties are given within a 95% confidence interval.

Table 5: Fitted data for the CFD results in Figure 20, using a fit function $f(D, T) = AD^{-\frac{1}{2}} + BD^{\frac{1}{2}} + C$ to give the sensor error. The units are identical to those in Tables 3 and 4. There is some discrepancy in the offset values.

	T_W (K)	Offset (K)	$D^{\frac{1}{2}}$ Coefficient	$D^{-\frac{1}{2}}$ Coefficient
CFD	373.120	$(2.20 \pm 0.71) \times 10^{-3}$	$(-7.43 \pm 0.53) \times 10^{-2}$	$(2.02 \pm 0.23) \times 10^{-4}$
Model	373.120	$(-9.84 \pm 5.85) \times 10^{-4}$	$(-6.94 \pm 2.08) \times 10^{-2}$	$(2.72 \pm 0.82) \times 10^{-4}$
CFD	173.260	$(0.45 \pm 2.84) \times 10^{-3}$	$(2.78 \pm 2.12) \times 10^{-2}$	$(1.37 \pm 0.90) \times 10^{-4}$
Model	173.260	$(4.22 \pm 1.27) \times 10^{-4}$	$(3.45 \pm 1.04) \times 10^{-2}$	$(1.08 \pm 0.32) \times 10^{-4}$

The CFD values are generally larger than the values predicted by the model. The exact reason for this is difficult to determine. In the original paper which develops the expression for Nu_{Cyl} [17], it is noted that the experimental measurements for the value of Nu_{Cyl} are lower than the values predicted by Eqn.6 for the Reynolds number range between 1,000 and 10,000. This may explain the generally lower errors predicted by this new model when compared to the CFD results. However, the nature of this discrepancy has not been quantified by the authors of the paper. It is also possible that the CFD results are slightly inaccurate due to the approximations of the radiation and fluid flow models. The thermodynamic properties of air used by the solver varied by less than 2% compared to the linear approximations of the theoretical model, so the theoretical approximations used in Section 3 are not likely to be a significant cause of the discrepancy. In any case, the CFD results are described appreciably by the theoretical model. An exact match of results using the model is not necessary, as this has little application to physical experiments. Given the large uncertainties due to sensor emissivity and the Nusselt number, model values will vary as different probes are used or the quality of the laminar air flow is disrupted, for example.

The zonal dependency graphs have provided an indicative method of predicting what behaviours will be expected at a given set of torus conditions. A small discrepancy is expected due to the offset of the CFD and theoretical model results. It has not been feasible to comprehensively investigate if the zonal dependency curves do in fact scale as T^{-2} in this project, due to computational limitations. However, the results show that for a similar value of $|T_W - T_A|$, an intermediary dependence is expected at 173.15 K in Figure 20 where a square root dependence is expected at 373.15 K in Figure 18. This is in line with the zonal dependency graph predictions.

In these simulations, it has been possible to specify an exact emissivity value for the sensor. Physical sensors have a variety of different surface emissivities with varying uncertainties, which will likely need to be estimated for experiments and calibrations. By operating the torus closer to ideal conditions, the error caused by radiative effects will be minimised, resulting in the lowest possible sensor emissivity uncertainty. Lower sensor emissivities will typically reduce the magnitude of the sensor errors, but will increase the size of the conditional zones, as shown in Figure 21. Research in 2020 has been carried out on methods of reducing radiation sensitivity of various sensors, which could be expanded to sensors used in the torus [10].

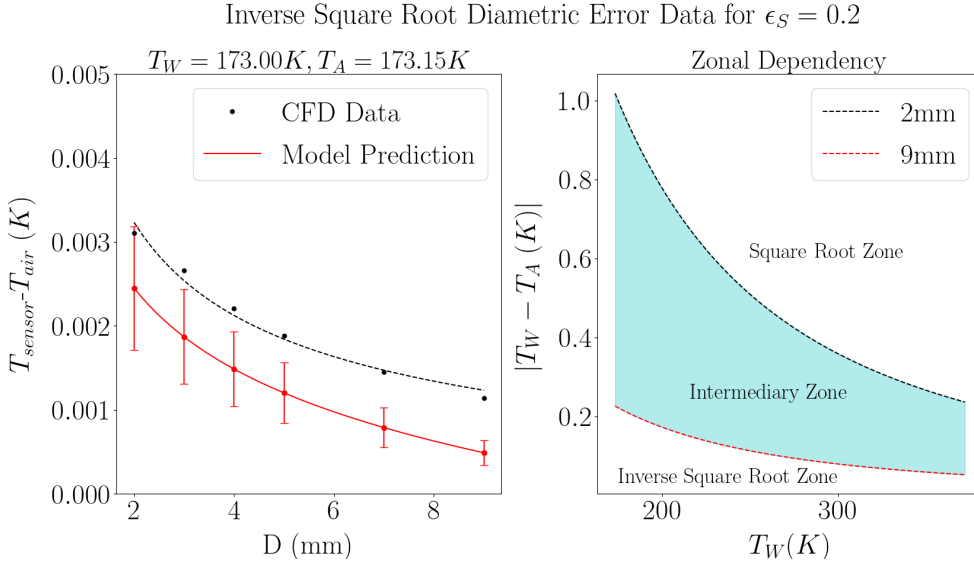


Figure 21: An inverse square root dependence is expected for a wider range of temperature conditions.

As it will not be possible to measure the thermophysical properties of air during a torus calibration, such properties must be inferred using the relations that have been developed in Section 3.2. To profile the behaviour of the torus as a calibration environment, sensors with similar, reasonably estimated emissivities of varying diameter can be used to profile the behaviour of the torus temperature conditions across the calibration temperature range required. The temperature measured by the sensors can be logged over time to determine the average temperature and stability of the air in the torus. If the fan heat output is constant, it is assumed the temperature reading will vary negligibly. Using the model, the sensor reading values can be fitted using model parameters, allowing for the air temperature to be calculated.

For this work, it is assumed that the torus temperature conditions will always remain in the inverse square root zone. This will likely be the case if the fan heat output is low and does not vary much over time. The drift of the average fan heat output over time may need to be evaluated over the course of the torus operating lifetime to account for deterioration of the mechanical parts of the fan which may change its heat output. Under these assumptions, a calibration process will involve at least two calibrated, standard probes and a UUT. The standard probe readings can provide an air temperature value using Eqn.33, and the error of the UUT can be determined.

4.2.4 Theoretical Uncertainty Budgets

Using the model values, theoretical uncertainty budgets are compiled and presented. The self-heating and radiative terms U_{SH} and U_{Rad} from Tables 1 and 9 are combined to give a term U_{Model} . A 4 mm sensor is chosen as the lowest diameter sensor for use in order to reduce excessive self-heating effects caused by lower diameter sensors.

Table 6: *A theoretical uncertainty budget for a torus calibration at 173.15 K assuming ideal torus conditions. This produces the lowest theoretical uncertainties achievable, according to the model.*

Symbol	Source of uncertainty	Unit	Value	Probability	Divisor	c_i	U_i
				\pm			
U_C	Calibration Uncertainty of Ref. PRT	mK	5	Normal	2	1	2.5
U_{Drift}	Ref. PRT Drift	mK	29	Rectangular	$\sqrt{3}$	1	16.7
U_{RB}	Resistance Bridge Uncertainty	mK	6	Rectangular	$\sqrt{3}$	1	3.5
U_{Axid}	Probe Axial Inhomogeneity	mK	1	Rectangular	$\sqrt{3}$	1	0.6
U_{BS}	Temp. stability	mK	1	Rectangular	$\sqrt{3}$	1	0.6
U_{Hys}	Hysteresis effect	mK	22	Rectangular	$\sqrt{3}$	1	12.7
U_{Model}	Radiation and self-heating effect	mK	5	Rectangular	$\sqrt{3}$	1	2.9
U_C	Combined Uncertainty			Normal			14.3
U	Expanded Uncertainty			Normal k=2			0.029 K

Table 7: *A theoretical uncertainty budget for a torus calibration at 373.15 K for ideal torus conditions.*

Symbol	Source of uncertainty	Unit	Value	Probability	Divisor	c_i	U_i
				\pm			
U_C	Calibration Uncertainty of Ref. PRT	mK	7	Normal	2	1	3.5
U_{Drift}	Ref. PRT Drift	mK	29	Rectangular	$\sqrt{3}$	1	16.7
U_{RB}	Resistance Bridge Uncertainty	mK	14	Rectangular	$\sqrt{3}$	1	8.1
U_{Axid}	Probe Axial Inhomogeneity	mK	0	Rectangular	$\sqrt{3}$	1	0.0
U_{BS}	Temp. stability	mK	0	Rectangular	$\sqrt{3}$	1	0.0
U_{Hys}	Hysteresis effect	mK	22	Rectangular	$\sqrt{3}$	1	12.7
U_{Model}	Radiation and self-heating effect	mK	5	Rectangular	$\sqrt{3}$	1	2.9
U_C	Combined Uncertainty			Normal			16.3
U	Expanded Uncertainty			Normal k=2			0.033 K

Ideal torus conditions allow for the expanded uncertainty to be reduced by 0.023 K at -100°C and by 0.074 K at $+100^{\circ}\text{C}$ (see Tables 1 and 9). The improvement may be even larger if stability and inhomogeneity values for the climatic chamber

were accounted for. The 5 mK value for U_{Model} represents a worst case value produced by the model, as it may be slightly lower for larger diameter sensors and lower temperatures. Table 10 shows another uncertainty budget with a 10 mK instability. This produces an expanded uncertainty of 0.048 K, a 0.059 K improvement over the climatic chamber.

It is clear from these results that there is a succinct advantage in using a torus submersion system. Reduction of uncertainties by up to 69% has been shown to be theoretically achievable. The potential reduction of uncertainties indicated by these uncertainty budgets is exceptional, and the results strongly suggest that pursuing further developments in the production of a torus calibration system is a worthwhile investment.

4.3 Pre-Lockdown Laboratory Work

4.3.1 Experimental Design

The procedure for testing the torus consists of setting the temperature of the external bath to a set point required, with the torus submerged in the bath liquid. Conditions within the torus reach equilibrium with the bath liquid as the internal fan rotates to maintain good thermal contact between the torus walls and the contained air. Capsule probes are placed in the torus ports such that they are not in contact with the walls of the torus. An SPRT in the bath liquid is used to determine the temperature T_W .

To investigate the viability of the torus for air temperature calibrations, a series of tests were completed and are currently planned for the period after COVID-19 restrictions are lifted. The aim of these tests is to profile the behaviour of the torus at a variety of conditions by determining the temperature stability and wall-air temperature difference.

4.3.2 Initial Testing With Electric Fan

The initial test measured the air velocity produced by the fan as a function of applied voltage. The CPU fans used had two wires for power and one wire that can be used to measure the voltage drop across the fan.

A larger voltage drop across the fan indicates a faster spin rate for the fan, and thus, a faster air velocity inside the torus. For this test, a Testo 425 Thermal Anemometer was inserted into one of the torus ports, ensuring that the hot-wire

of the anemometer was directly in the air flow. A voltmeter was connected to the fan to measure the fan voltage drop. A variable power supply was used to adjust the voltage supplied to the fan.

The anemometer averaging function was used to measure the average air velocity over a thirty second period. This sample was then recorded, with a total of five samples for each voltage. The standard deviation of each measurement is presented using a 95% confidence interval in Table 8. The Testo 425 Thermal Anemometer has an uncertainty provided by the manufacturer of around 4%. This may be improved upon by carrying out a calibration in a wind tunnel.

Table 8: *The data collected for each voltage setting on the power supply.*

Average Velocity (ms^{-1})	Average Voltage (V)
(0.63 ± 0.01)	(5.36 ± 0.09)
(0.67 ± 0.01)	(6.73 ± 0.05)
(0.77 ± 0.02)	(9.44 ± 0.02)
(0.94 ± 0.02)	(12.52 ± 0.05)

With the velocity-voltage pairs obtained, the internal speed of the fan could be measured indirectly using the voltage reading of an external voltmeter to infer the velocity. This allowed the anemometer to be removed from the torus, freeing up room for another sensor. The voltage output could also indicate if there were any issues with the fan rotation. Using a more advanced power supply could possibly reduce the deviation of the voltage and thus, reduce the uncertainty in the air velocity if required.

4.3.3 Internal Fan Heat Dissipation

The torus was submerged in methanol at $-80\text{ }^{\circ}C$ to test its function. After a short time operating, the fan stopped rotating, as the voltmeter was reading zero. The torus was removed and allowed to return to room temperature, where the same test was repeated without submerging the torus in liquid. The fan was no longer failing to rotate when the temperature had increased. During this repeat test however, an unexpected effect was discovered.

Due to the low volume of air, the fan was found to be heating up the air at a much faster rate than the heat transfer rate between the air and the torus walls.

This caused heating of the sensors. Larger velocities, which should in theory cool the sensor, were actually causing larger power usage by the fan, and consequently, faster increases in air temperature within the torus. This effect is shown by the data in Figure 22.

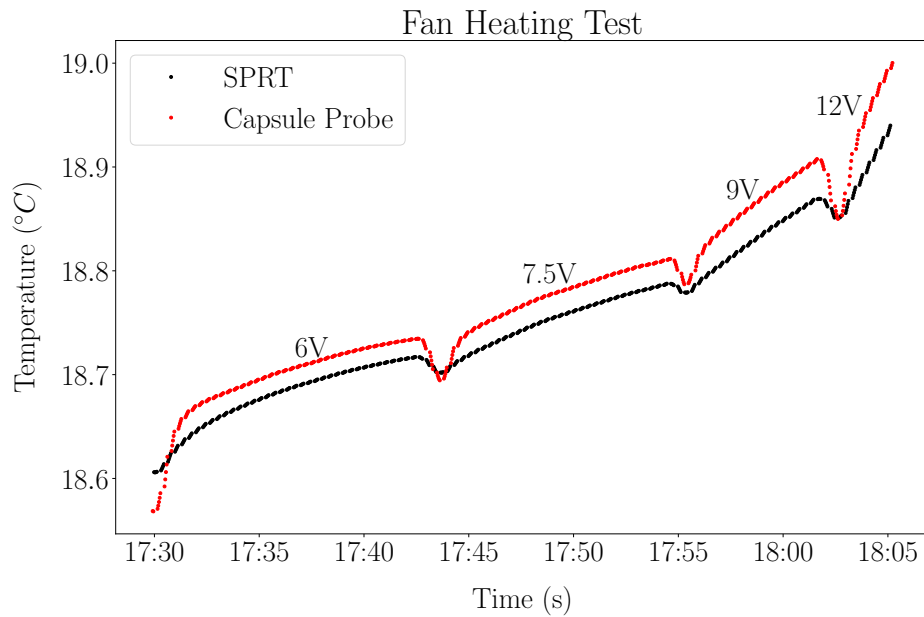


Figure 22: The sensor data recorded using a resistance bridge shows the fan air heating effect.

4.3.4 Ball Bearing Freeze Test

The fan rotation appeared to be affected by low temperatures. Upon disassembling the fan, the ball bearings were identified as a possible cause of this issue. To test this, the ball bearings were inserted into a glass tube and submerged in low temperature methanol. The ball bearings were rotated until a substantial increase in force was required to rotate them further. The tube was removed when the bearing could no longer be rotated. After a few seconds of warming in room temperature air, the bearings started to rotate again. It was therefore determined that the likely cause of the fan stoppage was the presence of dissimilar metals in the bearings, which caused thermal contraction at different rates due to their distinct coefficients of thermal expansion.

4.3.5 Solutions

It was not possible to find commercially available, suitably sized fans were designed to operate at temperatures below $-40\text{ }^{\circ}\text{C}$. It was not possible to find suitable cryogenic bearings. Using an external magnet is one possible idea, as this is typically the method for rotating objects such as fans. However, this technique is not possible due to the possible damage of electrical components in the liquid baths, and would likely affect current flow in the sensors.

One possible solution is to drive the fan using an external motor. Mechanical bushings are required to overcome the limitations posed by bearings at low temperatures. The motor can be attached to a drive shaft which is connected to the fan using a gearbox within the torus.

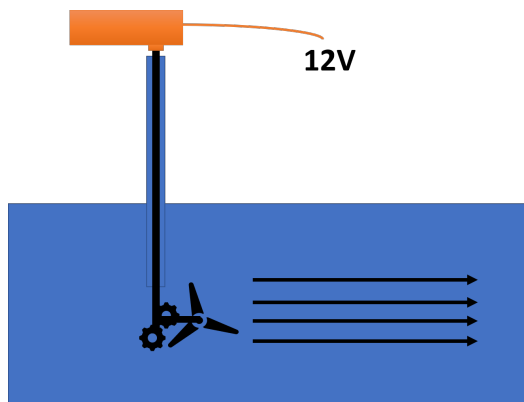


Figure 23: An externally driven fan will result in no electrical heating within the torus.

4.3.6 Gear-Driven Fan Design Process

Old plastic gears found in the lab were attached to the CPU fan by drilling holes in the fan housing and attaching shafts for the gears. A worm gear was attached to the end of a bike spoke which was used as a drive shaft to translate rotational energy from the external motor to the gears. The fan was removed from its bearing and a bushing was made using a metal tube. Since two of the torus ports are required at all times for probe insertion, only the small port is available for hosting the drive shaft. This port is off-centre by 9.5 mm. Additionally, there was only a $\sim 30\text{ mm}$ space between the torus walls and centre of rotation for the fan to place the gears and shafts. This added an extremely challenging constraint to design options.

To overcome this, the computer-aided design (CAD) program ‘Fusion 360’ was used with a laser-cutting machine to cut a plastic housing designed for the fan which allowed the required holes to be precisely cut. The laser cutter, despite being focused correctly, could not cut gear teeth to a sufficient standard, as the teeth deformed during the cutting process. The small gears were again used from old toys, and bevel gears were used in place of a worm gear as they appeared to increase the rotational speed of the fan. The bike spoke used for the drive shaft was replaced with a 3.5 mm length of silver steel to increase the sturdiness of the overall design.

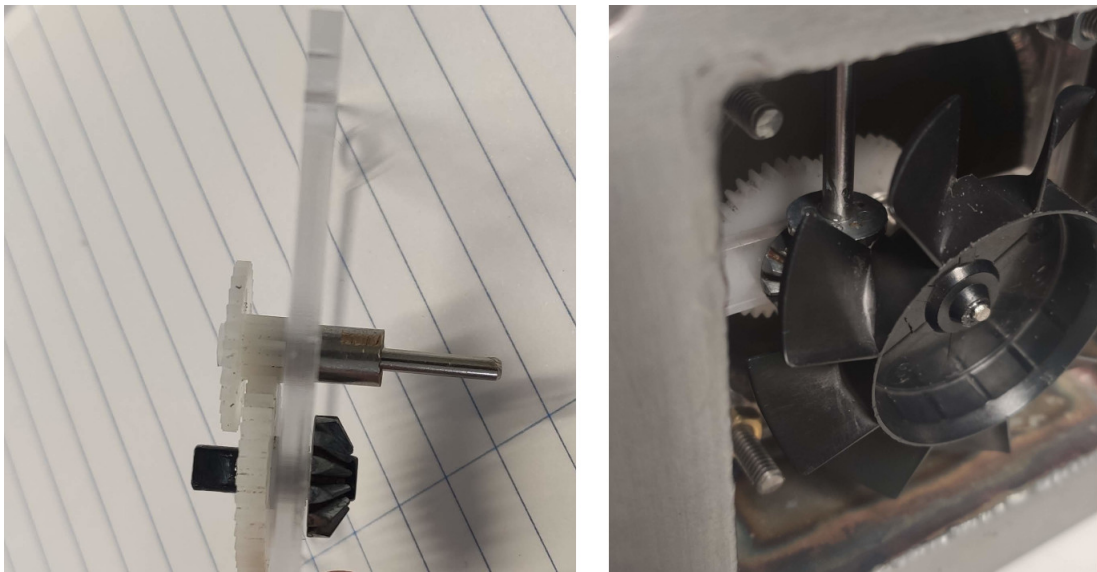


Figure 24: A perspex frame is used to keep the gears and bushing in place, with the fan attached.

4.3.7 Project Constraints and Solutions

The budget for producing the fan housing has been a primary limiting factor in the fan design and production process. A considerable amount of time was invested overcoming the challenges posed by the constrained space within the torus to place gears and by working with recycled gears and components. The design implementation in Figure 24 was successful in allowing the fan to be rotated by an external motor, but excessive vibrations were present. This was caused by the fan shaft and bushing diameters differing.

The addition of another perspex sheet to support the bushing and gears was the next planned action, however, access to the labs for further experimentation and

design was restricted by the pandemic lockdowns. Despite this, the current prototype should only require a few tweaks to become fully functioning for the experimental work required.

The use of high precision measuring equipment will likely require that vibrations are kept to an absolute minimum. This can be achieved by ensuring that the parts used have sub-millimetre dimensional precision. To overcome this design challenge, the use of precision engineering services may be useful. In particular, the production of appropriate gears, shafts and bushings could be a worthwhile investment. High thermal conductivity materials such as metals could be used instead of plastic, to promote conduction of heat away from the contact surfaces of the gears.

Frictional heating is also a major concern, as reduction of heat sources is the main objective with this design. A material with low thermal coefficient of expansion α , such as nylon, is therefore favourable. A length of material L_0 increases proportionally by a length ΔL with respect to a temperature change ΔT :

$$\Delta L = \alpha L_0 \Delta T \quad (\text{Eqn.35})$$

It is difficult to quantify the temperature increase caused by frictional heating caused by surface contact between gears and bushings. For this reason, it will be necessary to investigate these effects in future physical experiments.

4.3.8 Torus Heat Extraction

The rate at which heat is transferred through the torus walls will determine the wall-air temperature difference. A model for internal forced convection is used to quantify the theoretical requirements for ideal torus conditions:

$$\dot{Q} = hA\Delta T_{AM} \quad (\text{Eqn.36})$$

where h is the average heat transfer coefficient and ΔT_{AM} is the arithmetic mean temperature difference between the air and the torus walls, given by:

$$T_{AM} = T_s - \frac{T_i + T_e}{2} \quad (\text{Eqn.37})$$

with T_i and T_e as an inlet and exit temperatures, respectively, for a length of pipe. For the torus, T_i will denote the air temperature flowing out of the fan (where it is cooled), and T_e will denote the air temperature flowing into the fan (where it is

heated). The log mean temperature difference, described in Heat and Mass Transfer [9], more accurately accounts for the exponential decay rate of local temperature as the flow progresses through a pipe. However, for the small temperature differences in the torus, T_{AM} is suitable. For a 1 mK uncertainty between the values of T_A and T_W , the values of $T_e = T_W + 1$ mK and $T_i = T_e + 1$ mK produce a value $\Delta T_{AM} = 0.0015$ K. The torus length of 0.56 m and diameter 60 mm give a total surface area of 0.11 m^2 . For the value h , a constant Nu value of 3.66 is used due to constant temperature wall conditions [9]:

$$h = \frac{Nu \cdot k}{D} = \frac{3.66 \cdot k(T_A)}{0.06m} \quad (\text{Eqn.38})$$

This gives $h = 1.90 \pm 0.02$ at $+100$ °C and $h = 0.98 \pm 0.02$ at -100 °C in units $Wm^{-2}K^{-1}$. The lowest rate of heat transfer through the walls is therefore:

$$\dot{Q} = (1.62 \pm 0.03) \times 10^{-4}W \quad (\text{Eqn.39})$$

The maximum sensor heating rate is around 80% of this value. It is therefore necessary that the heat output from fan components is around $3 \times 10^{-5}W$ to ensure the 1mK uncertainty is achieved. This may be difficult to achieve with multiple sensors and limited control over the fan heating rate. It may be necessary to increase the 1mK tolerance depending on the exact limitations of a given set up, resulting in a higher overall uncertainty.

5 Conclusions and Future Perspectives

The primary aim of this project was to develop a thermodynamic model for precision temperature metrology using empirical correlations and literature data. This model has been successfully developed and supported by CFD simulations. The model results have shown that significantly smaller uncertainties are achievable for air calibrations, with uncertainty reductions of up to 69%. A submersible ‘torus’ system has been outlined and shown to be a viable environment to achieve these results, at a fraction of the cost of a climatic chamber.

The theoretical model has uniquely predicted an inverse square root diametric-error relationship and a similar intermediary behaviour, which are quantitatively described using zonal dependency graphs. These zonal dependency graphs provide a comprehensive model of expected diametric error dependences at all temperature con-

ditions in the range of $-100\text{ }^{\circ}\text{C}$ to $+100\text{ }^{\circ}\text{C}$, and successfully predict the square root diametric-error dependence investigated in previous works [5].

Experimental work was carried out to reduce the heating effect of an electric fan used in the torus design. This involved the successful development of a gear-driven fan. Due to pandemic lockdowns, access to laboratories for testing of this newly developed fan were postponed. Despite this, the mode results provide a significant indication that even with a non-adiabatic fan, exceptionally small uncertainties are achievable with the torus system.

Improvements to the model may be achieved with further research into the Nusselt number correlation used in Eqn.6. This correlation has a 30% uncertainty which may conceivably be improved upon. The complex fitting process required to describe the related experimental data may be assisted using the modern model discovery tools developed for the Julia programming language recently [18]. The small discrepancy between CFD results and model predictions may be explained with a better understanding of the uncertainties in Eqn.6.

It is hoped that this work can be used to push the boundaries of what is achievable in air temperature metrology, and provide a theoretical basis for future technologies that require precise system temperature control.

References

- [1] H. Preston-Thomas, *The International Temperature Scale of 1990 (ITS-90)*, 1990. [Online]. Available: [https://www.nist.gov/system/files/documents/pml/div685/grp01/ITS-90__metrologia.pdf](https://www.nist.gov/system/files/documents/pml/div685/grp01/ITS-90\metrologia.pdf) (visited on 10/29/2020).
- [2] J. A. Sousa and A. S. Ribeiro, *THE CHOICE OF METHOD TO THE EVALUATION OF MEASUREMENT UNCERTAINTY IN METROLOGY*. 2009, ISBN: 9789638841001.
- [3] W. L. Tew and G. F. Strouse, “Standard Reference Materials ® Standard Reference Material 1750: Standard Platinum Resistance Thermometers, 13.8033 K to 429.7485 K,” Tech. Rep.
- [4] G. E. Daniels, “Measurement of Gas Temperature and the Radiation Compensating Thermocouple,” Tech. Rep. 6, 1968, pp. 1026–1035. DOI: 10.1175/1520-0450(1968)007<1026:MOGTAT>2.0.CO;2. [Online]. Available: <http://journals.ametsoc.org/jamc/article-pdf/7/6/1026/4975330/1520-0450>.
- [5] M. De Podesta, R. Underwood, L. Bevilacqua, and S. Bell, “Air temperature measurement challenges in precision metrology,” in *Journal of Physics: Conference Series*, vol. 1065, Institute of Physics Publishing, 2018. DOI: 10.1088/1742-6596/1065/12/122027.
- [6] W. O. Library, R Underwood, T Gardiner, A Finlayson, J Few, J Wilkinson, S Bell, J Merrison, J. J. Iverson, and M De Podesta, “A combined non-contact acoustic thermometer and infrared hygrometer for atmospheric measurements,” *METEOROLOGICAL APPLICATIONS Meteorol. Appl.*, vol. 22, pp. 830–835, 2015. DOI: 10.1002/met.1513.
- [7] B. Feng, Y. Sun, X. Yang, S. Li, J. Tu, and S. Jiang, “Characteristics of Helium Gas with High Temperature and High Pressure Flowing through a 90-Degree Elbow,” *ISRN Power Engineering*, vol. 2014, pp. 1–6, 2014, ISSN: 2090-4665. DOI: 10.1155/2014/764283.
- [8] V. Žužek and I. Pušnik, “Calibration of Air Thermometers in a Climatic Chamber and Liquid Baths B Vincencij Žužek,” *International Journal of Thermophysics*, vol. 38, p. 100, 2017. DOI: 10.1007/s10765-017-2234-6.

- [9] Y. A. Cengel and A. J. Ghajar, *Heat and Mass Transfer: Fundamentals and Applications*, 5th ed. New York, NY: McGraw-Hill Professional, 2014.
- [10] H. Lundström and M. Mattsson, “Radiation influence on indoor air temperature sensors: Experimental evaluation of measurement errors and improvement methods,” *Experimental Thermal and Fluid Science*, vol. 115, p. 110 082, 2020, ISSN: 08941777. DOI: 10.1016/j.expthermflusci.2020.110082. [Online]. Available: <https://linkinghub.elsevier.com/retrieve/pii/S0894177719313822>.
- [11] V. Batagelj, J. Bojkovski, and J. Drnovšek, “Methods of reducing the uncertainty of the self-heating correction of a standard platinum resistance thermometer in temperature measurements of the highest accuracy,” *Measurement Science and Technology*, vol. 14, no. 12, pp. 2151–2158, 2003, ISSN: 09570233. DOI: 10.1088/0957-0233/14/12/016. [Online]. Available: <https://iopscience.iop.org/article/10.1088/0957-0233/14/12/016><https://iopscience.iop.org/article/10.1088/0957-0233/14/12/016/meta>.
- [12] S. Burt and M. Podesta, “Response times of meteorological air temperature sensors,” *Quarterly Journal of the Royal Meteorological Society*, vol. 146, no. 731, pp. 2789–2800, 2020, ISSN: 0035-9009. DOI: 10.1002/qj.3817. [Online]. Available: <https://onlinelibrary.wiley.com/doi/10.1002/qj.3817>.
- [13] E. Erell, V. Leal, and E. Maldonado, “Measurement of air temperature in the presence of a large radiant flux: An assessment of passively ventilated thermometer screens,” *Boundary-Layer Meteorology*, vol. 114, no. 1, pp. 205–231, 2005, ISSN: 00068314. DOI: 10.1007/s10546-004-8946-8. [Online]. Available: <https://link.springer.com/article/10.1007/s10546-004-8946-8>.
- [14] I. Demirdžić and M. Perić, “Finite volume method for prediction of fluid flow in arbitrarily shaped domains with moving boundaries,” *International Journal for Numerical Methods in Fluids*, vol. 10, no. 7, pp. 771–790, 1990, ISSN: 0271-2091. DOI: 10.1002/fld.1650100705. [Online]. Available: <http://doi.wiley.com/10.1002/fld.1650100705>.
- [15] ANSYS FLUENT 12.0/12.1 Documentation. [Online]. Available: <https://www.afs.enea.it/project/neptunius/docs/fluent/index.htm> (visited on 03/21/2021).

- [16] ANSYS FLUENT 12.0 Theory Guide - 5.3.7 Surface-to-Surface (S2S) Radiation Model Theory. [Online]. Available: <https://www.afs.enea.it/project/neptunius/docs/fluent/html/th/node116.htm> (visited on 03/26/2021).
- [17] S. W. Churchill and M. Bernstein, “A correlating equation for forced convection from gases and liquids to a circular cylinder in crossflow,” *Journal of Heat Transfer*, vol. 99, no. 2, pp. 300–306, 1977, ISSN: 15288943. DOI: 10.1115/1.3450685.
- [18] C. Rackauckas, Y. Ma, J. Martensen, C. Warner, K. Zubov, R. Supekar, D. Skinner, and A. Ramadhan, “Universal differential equations for scientific machine learning,” *arXiv preprint arXiv:2001.04385*, 2020.

Appendix A: Risk Assessment

Student Name:	Paul McBrien
Student Number:	17715295
Project Title:	A Semi-Empirical Theoretical Model For Precise Air Temperature Metrology
Main Project Working Location:	National Metrology Laboratory, Glasnevin
Supervisor Name:	Dubhaltach MacLochlainn
This project involved some experimental work with no significant risks, and all risks were identified and managed according to safety guidelines in the National Metrology Laboratory.	
<ol style="list-style-type: none">1. Risk of skin burn due exposure to low temperature liquid2. Risk of inhalation of fumes3. Risk of tripping over cables	

Hazard Identification & Risk Assessment

Page 1 of 1

Prepared by:

Paul McBrien

07/12/2020

School/Unit/Faculty name: School of Physics

07/12/2020

Groups affected: Student

Hazards	Is the Hazard present? Y/N	What is the risk?	Controls - Controls in place to reduce risks	Is the control in place? Y/N	Likelihood	Severity	Risk Rating (L x S)	J/W/H	Person(s) Responsible for Control Measure Implementation
Loose Cables	Y	Injuries caused by tripping over cables.	Use of cable ties where possible.	Y	3	1	3	L	Paul McBrien, Dubhaltach MacLochlainn
Exposure To Chemicals	Y	Skin contact with low temperature methanol	Use of Personal Protective Equipment must be worn to prevent skin irritation/freeze burns.	Y	1	2	2	L	Paul McBrien, Dubhaltach MacLochlainn
	Y	Inhalation of methanol vapour	Fume hoods must be used at all times when using equipment with methanol.	Y	1	2	2	L	Paul McBrien, Dubhaltach MacLochlainn
Laser Machine	Y	Inhalation of fumes caused by burning plastic	Use of extraction fan at all times when operating the laser machine.	Y	1	3	3	L	Paul McBrien
Live Wires	Y	Electric shock due to unearthing wire.	Ensure all electrical equipment is checked to ensure correct fuse functioning.	Y	1	1	1	L	Paul McBrien, Dubhaltach MacLochlainn

Appendix B: Supplementary Figures and Tables

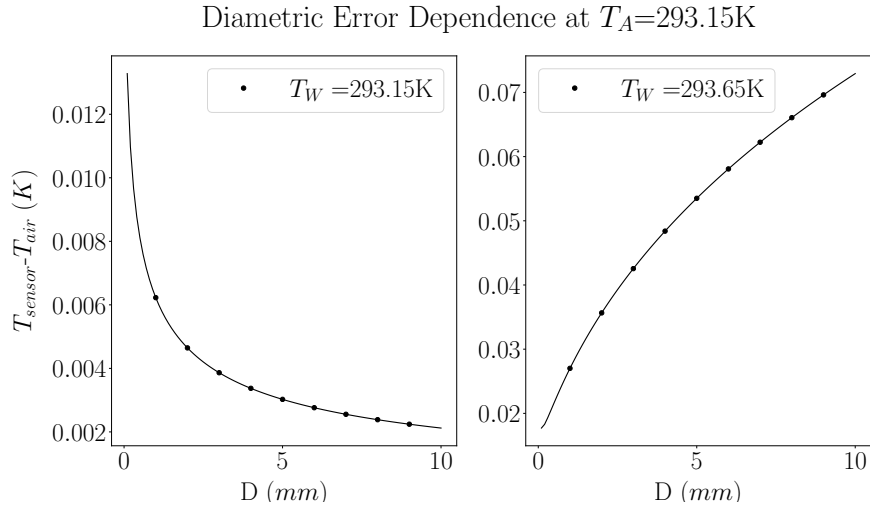


Figure 25: At $T_A = 20.000 \text{ } ^\circ\text{C}$, the model values for the temperature error variation with diameter using the default parameter values, with $T_W = 20.000 \text{ } ^\circ\text{C}$ and $T_W = 20.500 \text{ } ^\circ\text{C}$ for $D^{-\frac{1}{2}}$ and $D^{\frac{1}{2}}$ proportionality, respectively.

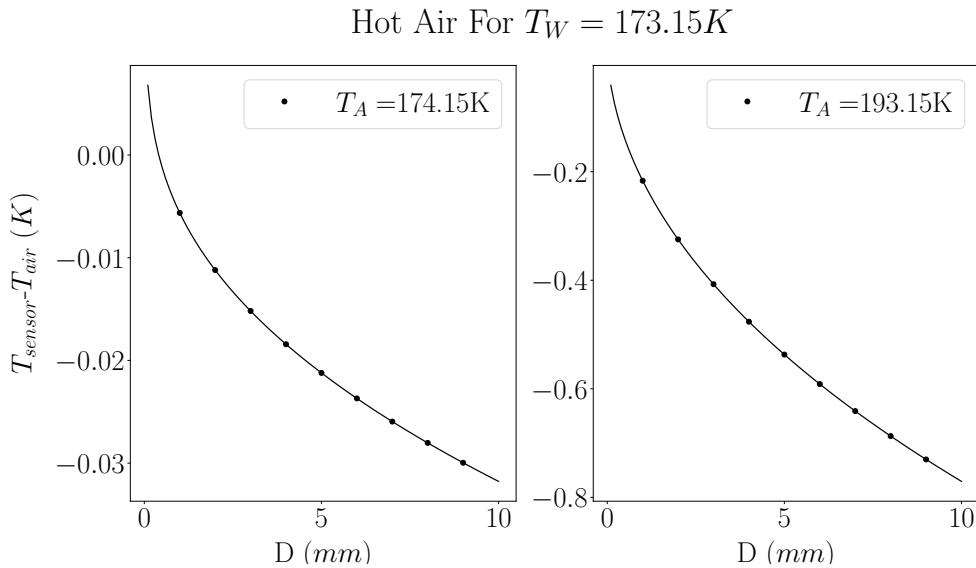


Figure 26: A square root dependence is expected for larger wall-air temperature differences.

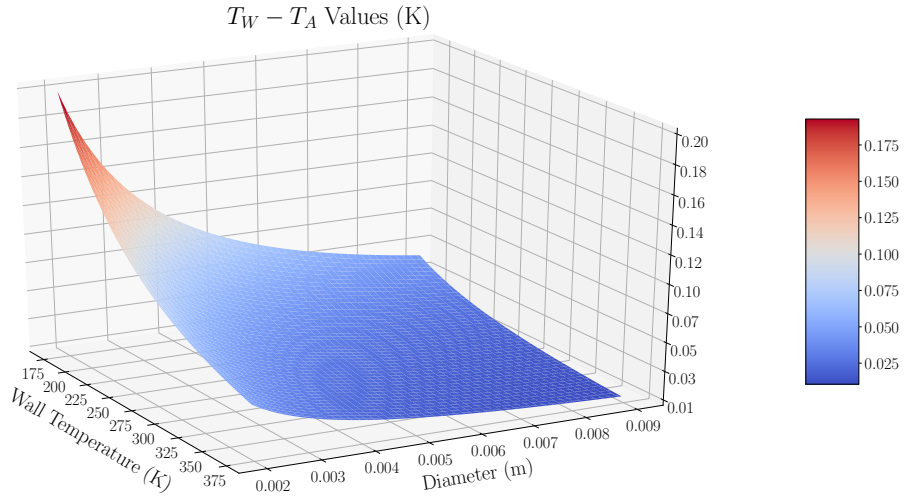


Figure 27: All possible inverse T^2 curves that describe the torus zonal dependency graphs, with $T_W - T_A$ on the vertical z -axis.

Table 9: A sample uncertainty budget for an air temperature calibration at 373.15 K, which is used for calibrations carried out in a climatic chamber. The values for the temperature stability and homogeneity are omitted, but typically lead to an expanded uncertainty on the order of 0.1 K.

Symbol	Source of uncertainty	Unit	Value ±	Probability Distribution	Divisor	c_i	U_i
U_C	Calibration Uncertainty of Ref. PRT	mK	7	Normal	2	1	3.5
U_{Drift}	Ref. PRT Drift	mK	29	Rectangular	$\sqrt{3}$	1	16.7
U_{RB}	Resistance Bridge Uncertainty	mK	14	Rectangular	$\sqrt{3}$	1	8.1
U_{Axid}	Probe Axial Inhomogeneity	mK	0	Rectangular	$\sqrt{3}$	1	0.0
U_{SH}	Self heating effect	mK	12	Rectangular	$\sqrt{3}$	1	6.9
U_{BS}	Temp. stability	mK	0	Rectangular	$\sqrt{3}$	1	0.0
U_{Hys}	Hysteresis effect	mK	22	Rectangular	$\sqrt{3}$	1	12.7
U_{Rad}	Radiation effect	mK	83	Rectangular	$\sqrt{3}$	1	47.8
U_C	Combined Uncertainty			Normal			53.4
U	Expanded Uncertainty			Normal k=2			0.107 K

Table 10: A theoretical uncertainty budget for a torus calibration at 373.15 K with 10 mK instability. The values for the homogeneity is estimated at 1 mK as a variation in torus temperature should affect all air within the torus at a similar rate.

Symbol	Source of uncertainty	Unit	Value ±	Probability Distribution	Divisor	c_i	U_i
U_C	Calibration Uncertainty of Ref. PRT	mK	7	Normal	2	1	3.5
U_{Drift}	Ref. PRT Drift	mK	29	Rectangular	$\sqrt{3}$	1	16.7
U_{RB}	Resistance Bridge Uncertainty	mK	14	Rectangular	$\sqrt{3}$	1	8.1
U_{Axz}	Probe Axial Inhomogeneity	mK	1	Rectangular	$\sqrt{3}$	1	0.6
U_{BS}	Temp. stability	mK	10	Rectangular	$\sqrt{3}$	1	5.8
U_{Hys}	Hysteresis effect	mK	22	Rectangular	$\sqrt{3}$	1	12.7
U_{Model}	Radiation and self-heating effect	mK	6	Rectangular	$\sqrt{3}$	1	3.5
U_C	Combined Uncertainty			Normal			23.8
U	Expanded Uncertainty			Normal k=2			0.048 K

Inverse Square Root Diametric-Error Derivation

Using Equations from Sections 2.3 and 3:

$$\begin{aligned} \dot{Q}_{Flow} = hA(T_S - T_A) &\implies (T_S - T_A) = \frac{\dot{Q}_{Flow}}{hA} = \frac{\dot{Q}_{Flow}D}{kNu_{Cyl}A} \\ &\implies (T_S - T_A) \propto \frac{\dot{Q}_{Flow}D}{kV^{\frac{1}{2}}D^{\frac{1}{2}}\pi DL} \propto \frac{\dot{Q}_{Flow}D}{V^{\frac{1}{2}}D^{\frac{1}{2}}D} \\ &\implies (T_S - T_A) \propto \frac{\dot{Q}_{Flow}}{V^{\frac{1}{2}}D^{\frac{1}{2}}} \end{aligned}$$

This differs to the the Equation 15 in [5], which is:

$$(T_S - T_A) \propto \dot{Q}_{Flow} \frac{D^{\frac{1}{2}}}{V^{\frac{1}{2}}}$$

It is possible to achieve this square root dependency only if multiple of D is present, such as with an area term A .

Appendix C: Code Functions

Theoretical Model Code

```
import pandas as pd
import numpy as np
import matplotlib.pyplot as plt
from uncertainties.umath import *
from scipy.optimize import curve_fit
from uncertainties import ufloat
import scipy
from scipy.stats import *

I = 1e-3
es = 1
cp_meanerror = ufloat(986,22)
cp_mean = 986
sigma = 5.6704e-8

def R(T):
    #Determined by regression of resistance-temperature data
    return (0.39612052145787646*T-8.291111694154438)

def conductivity_kerror(Ta):
    return ufloat(7.521e-05,8.307e-07)*Ta+ufloat(3.019e-03,2.456e-04)
def conductivity_k(Ta):
    return 7.521e-05*Ta+3.019e-03
def transfer_coefficient(Ta,V, D):
    return conductivity_k(Ta)*NuCyl(Ta,V,D)/D
def transfer_coefficienterror(Ta,V, D):
    return conductivity_kerror(Ta)*NuCylerror(Ta,V,D)/D
def density_function(Ta):
    #Using STP
    rho = (101325*28.97/1000)/(8.3145*(Ta))
    return rho
def dynamic_viscosity_functionerror(Ta):
```

```

        return ufloat(4.855e-08,1.452e-09)*Ta+ufloat(3.907e-06,4.295e-07)

def dynamic_viscosity_function(Ta):
    return 4.855e-08*Ta+3.907e-06

def kinematic_viscosity_function(Ta):
    return dynamic_viscosity_function(Ta)/density_function(Ta)

def kinematic_viscosity_functionerror(Ta):
    return dynamic_viscosity_functionerror(Ta)/density_function(Ta)

def Re(V,D,Ta):
    return (V*D)/kinematic_viscosity_function(Ta)

def Reerror(V,D,Ta):
    return (V*D)/kinematic_viscosity_functionerror(Ta)

def Pr(Ta):
    return dynamic_viscosity_function(Ta)*cp_mean/conductivity_k(Ta)

def Prerror(Ta):
    return dynamic_viscosity_functionerror(Ta)*cp_meanerror/conductivity_kerror(Ta)

def NuCyl(T,V,D):
    Reynolds = Re(V,D,T)
    Prandtl = Pr(T)
    term2 = (0.62*(Reynolds**0.5)*(Prandtl)**(1/3))/(1+(0.4/Prandtl)**(2/3))**(1/4)
    term3 = (1+(Reynolds/282000)**(5/8))**(4/5)
    ans = 0.3 + term2 + term3
    return ans

def NuCylerror(T,V,D):
    Reynolds = Reerror(V,D,T)
    Prandtl = Prerror(T)
    term2 = (0.62*(Reynolds**0.5)*(Prandtl)**(1/3))/(1+(0.4/Prandtl)**(2/3))**(1/4)
    term3 = (1+(Reynolds/282000)**(5/8))**(4/5)
    ans = 0.3 + term2 + term3
    return ans*ufloat(1,0.3) #to add 30 percent error from literature

def TsFunc(D, L, V, I, Tw, Ta, es):
    A = np.pi*D*L
    h = transfer_coefficient(Ta,V,D)
    electrical = I**2*R(Ta)
    area = np.pi*D*L
    a = es*sigma*A

```

```

d = -(h*A*Ta+electrical+es*sigma*A*Tw**4)
quadratic_roots = np.roots([a,0,0,h*A,d])
for root in quadratic_roots:
    if root.imag == 0:
        Ts = root.real
return Ts

def TsFuncerror(D, L, V, I, Tw, Ta, es):
    #Using approximation of quartic function
    A = np.pi*D*L
    h = transfer_coefficienterror(Ta,V,D)
    electrical = I**2*R(Ta)
    direct = 0
    numerator = electrical+direct+4*sigma*es*A*Tw**4+h*A*Ta
    denom = h*A + 4*sigma*es*A*Tw**3
    ans = numerator/denom
    return ans

TsFunc = np.vectorize(TsFunc) #make function work better with Numpy

def sensorHeatRate(I,T,D,L):
    ans = (I**2*R(T))/(np.pi*D*L)
    return ans

def sensorVolumeHeat(D,T):
    ans = (I**2*R(T))/(np.pi*(D/2)**2)
    return ans

```